A lattice Boltzmann investigation of steady-state fluid distribution, capillary pressure and relative permeability of a porous medium: effects of fluid and geometrical properties

Zi Li [1], Sergio Galindo-Torres [2], Guanxi Yan [3], Alexander Scheuermann [3], Ling Li [1]

[1] Research Group on Complex Processes in Geo-Systems, School of Civil Engineering, The University of Queensland, Brisbane, QLD 4072, Australia

[2] Department of Civil Engineering and Industrial Design, The University of Liverpool, Liverpool, L69 3BX, United Kingdom.

[3] Geotechnical Engineering Centre, School of Civil Engineering, The University of Queensland, Brisbane QLD 4072, Australia.

Abstract

Simulations of simultaneous steady-state two-phase flow in the capillary force-dominated regime were conducted using the state-of-the-art Shan-Chen multi-component lattice Boltzmann model (SCMC-LBM) based on two-dimensional porous media. We focused on analysing the fluid distribution (*i.e.*, WP fluid-solid, NP fluid-solid and fluid-fluid interfacial areas) as well as the capillary pressure versus saturation curve which was affected by fluid and geometrical properties (*i.e.*, wettability, adhesive strength, pore size distribution and specific surface area). How these properties influenced the relative permeability versus saturation relation through apparent effective permeability and threshold pressure gradient was also explored. The SCMC-LBM simulations showed that, a thin WP fluid film formed around the solid surface due to the adhesive fluid-solid interaction, resulting in discrete WP fluid distributions and reduction of the WP fluid mobility. Also, the adhesive interaction provided another source of capillary pressure in addition to capillary force, which, however, did not affect the mobility of the NP fluid. The film fluid effect could be enhanced by large adhesive strength and fine pores in heterogeneous porous media. In the steady-state infiltration, not only the NP fluid but also the WP fluid were subjected to the capillary resistance. The capillary pressure effect could be alleviated by decreased wettability, large average pore radius and improved fluid connectivity in heterogeneous porous media. The present work based on the SCMC-LBM investigations elucidated the role of film fluid as well as capillary pressure in the two-phase flow system. The findings have implications for ways to improve the macroscopic flow equation based on balance of force for the steady-state infiltration.

Keywords: Steady-state, fluid distribution, capillary pressure, relative permeability, lattice Boltzmann model.

1. Introduction

The steady-state infiltration through porous media (*i.e.*, the simultaneous flow of two immiscible fluids at the dynamic equilibrium) is commonly encountered in natural and industrial processes, such as, non-aqueous-phase liquid (NAPL) migration [1~2] and enhanced oil recovery [3~4]. The flow pattern features the competition between local drainage and local imbibition associated with breakdown and coalesce of fragmented fluid clusters, and the spatiotemporally invariant fluid saturation, fluid flux, capillary pressure and interfacial area at the statistical equilibrium [5~10]. Modelling of such two-phase flow process at the macroscale relies on the typical constitutive relationships, including relative permeability ($k_{r\sigma}$) and capillary pressure (p_c) as function of fluid saturation (s_w) as defined below [11, 12]

$$k_{r\sigma}(s_w) = \frac{k_\sigma}{k_{sat}}, \quad (1)$$

$$p_c\ (s_w) = p_n - p_w, \quad (2)$$

where, $\sigma = w, n$ denotes wetting phase (WP) or non-wetting phase (NP) fluid; and k_σ, k_{sat} and p_σ are effective permeability in the extended two-phase Darcy equation, intrinsic permeability and fluid pressure, respectively. These two equations provide an averaged representation of fluid and geometrical properties inside a representative elementary volume (REV) of the given solid-WP fluid-NP fluid system. However, they are not truly constitutive, in the sense that, $k_{r\sigma}(s_w)$ relation and $p_c(s_w)$ curve are both strongly hysteretic with respect to the flow conditions (*i.e.*, steady-state infiltration or transient displacement) [11, 13~15], and the capillary number [11, 16~18]. In practice, it is questionable either to apply the $k_{r\sigma}(s_w)$ relation measured in the steady-state infiltration to predict the transient displacement behavior, or to utilize the $p_c(s_w)$ curve acquired from the displacement experiment for the steady-state flow analysis [11].

Film fluid around the solid surface and capillary pressure have been identified as important factors in controlling the $k_{r\sigma}(s_w)$ relation in the capillary force-dominated regime [19, 20]. As the focus of this study, both factors are intrinsic to the two-phase flow system in the coupled thermo-hydrodynamic steady-state infiltration. *Longmuir* [21] suggested that, the adhesive interaction between fluid molecules in the pore and solid particles at the surface is capable of generating a WP fluid film around the solid surface, which reduces the WP fluid mobility (the degree of easiness for the fluid movement) and makes the fluid behave in a non-Newtonian way at the macroscale. *Benzi et al.* [22] observed that, the repulsive fluid-solid interaction compelled the fluid particles to be away from the solid surface, and the fluid density and viscosity drop rapidly near the solid wall causing the apparent slippage behavior. To account for the macroscale effects of capillary force on the two-phase fluid flow, *Hassanizadeh and Gray* [23, 24] proposed an advanced two-phase flow theory by introducing the fluid-fluid interfacial area as a new independent state variable. The proposed Darcy equation included gradients of fluid saturation and fluid-fluid interfacial area as the driving forces. The interfacial areas can be determined through the image analysis technique and calculated as follows [25, 26],

$$A_{nw}(s_w) = \frac{(A_n + A_w - A_s)}{2},\ A_{ws}(s_w) = A_w - A_{nw},\ A_{ns}(s_w) = A_n - A_{nw}, \quad (3)$$

where, A_s, A_w, and A_n denote the specific surface areas of solid grains, WP fluid and NP fluid, respectively; and A_{nw}, A_{ws} and A_{ns} represent the fluid-fluid, WP fluid-solid and NP fluid-solid interfacial areas, respectively.

The two-phase flow process during the steady-state infiltration can be supposed to be the result of an interplay between gravity and adhesive, capillary, and viscous forces at the pore scale. As shown in Fig. 1, the individual WP and NP fluid packets in the two-phase flow system may form connected pathways or isolated in the form of bridges or ganglion. As given by the extended two-phase Darcy equation [12], the stationary solid exerts viscous force on the two flowing fluids tangentially on the fluid-solid interfacial area. Adhesive or repulsive force is imposed by the solid surface to the adjacent fluids normally [21, 22]. On the fluid-fluid interfacial area, both normal capillary resistance to the flow of two neighbouring fluid packets [23, 24] and tangential viscous coupling between the two flowing fluids occur. In the capillary force-dominated regime, viscous coupling process is not significant; and hence adhesive, capillary and viscous forces dissipate almost all the input energy through the interfacial areas. At the dynamic equilibrium where the macroscopic state variables reach the steady state

[5~10], a new macroscopic flow equation based on balance of force with consideration of the interfacial areas and the local parametrized pore scale forces can be potentially established.

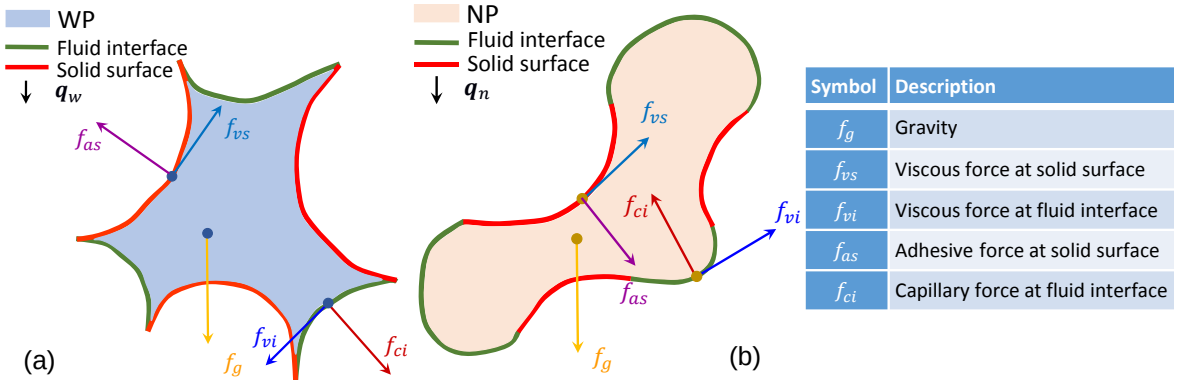

Symbol	Description
f_g	Gravity
f_{vs}	Viscous force at solid surface
f_{vi}	Viscous force at fluid interface
f_{as}	Adhesive force at solid surface
f_{ci}	Capillary force at fluid interface

Fig. 1. Representation of interfacial areas and pore scale forces for the WP (a) and NP (b) fluid packets, drawn from the configuration of two immiscible fluids inside a REV. For simplicity, the gravity is indicated as the flow driver.

Nevertheless, so far attention has rarely been paid to how fluid and geometrical properties determine the interfacial areas, the film fluid and the capillary pressure at the steady state. On the other hand, a large volume of literature concerned with the steady-state relative permeability subject to these properties have been published in the past few decades.

As the wettability increased, the WP relative permeability at each saturation decreased [27~29] due to the WP fluid in contact with more solid surface, while the NP relative permeability increased for the sphere-pack porous medium [27] and carbon paper gas diffusion layer [28] but decreased for the bead-pack system [29]. The different behaviors of the NP relative permeability under the varying wettability could be attributed to two opposing mechanisms. With increased wettability, less NP fluid-solid interfacial area with less viscous resistance dominated the packing spheres [27] and gas diffusion layer [28], whereas more disconnected NP fluid with larger capillary resistance was dominant in the packing beads [29]. Furthermore, the rock wettability can be altered by the distribution of brine and oil. As a result, the effect of mixed wettability on the relative permeabilities of two immiscible fluids becomes more complex [29]. When evaluating the data of fluid flux versus pressure gradient for saturated clays, *Swartzendruber* [30] was surprised to find a few positive pressure gradient intercepts of the fitted lines for the soils with more clay content. Subsequently, *Miller and Low* [31] and *Prada and Civan* [32] observed the threshold pressure gradient in clay and sandstone, respectively, below which the fluid could not flow. The nonlinear flow phenomenon was supposed to be due to reduced film fluid mobility and macroscale non-Newtonian fluid flow behavior caused by the adhesive fluid-solid interaction [21]. Further, *Hao et al.* [19] and *Dou et al.* [20] suggested that, the threshold pressure gradient phenomenon in the two-phase flow process resulted from two aspects, film fluid effect and capillary resistance, offering a complete interpretation for the dependence of the $k_{r\sigma}(s_w)$ relation on capillary number [11, 16~18].

Studies have been carried out on various pore size distributions generated in homogeneous and heterogeneous porous media [33]. It was demonstrated that, the NP fluid in heterogeneous porous media could more readily become continuous experiencing less capillary trapping, and thus the NP relative permeability in heterogeneous porous media was significantly higher than that in homogeneous porous media [33]. In contrast, the WP fluid in heterogeneous porous media was more discretely distributed with more extensive contacts with solid surface, and hence the WP relative permeability in heterogeneous porous media

was slightly lower [33]. With increasing specific solid surface area [34, 35], the NP relative permeability decreased significantly, while the WP relative permeability remained almost invariant. This was because the WP fluid became more connected to not only itself but also solid surface, and the resulting effects cancelled each other to a large extent, causing little change in the WP relative permeability. Also, a higher pressure gradient was needed for the fully connected NP fluid flow to reach the linear flow regime due to higher fraction of small pore sizes [36]. The effects of fluid and geometrical properties on the fluid flow behavior were found to be strongly coupled [19, 20]. For example, a high fraction of fine pores in heterogeneous porous media facilitated the generation of film fluid, and the small pore radius in homogeneous porous media favored the capillary resistance.

Compared with the constitutive relationships, the pore scale configuration of two immiscible fluids would provide fundamental understandings of the macroscopic transport behavior [5~10, 37~40]. In addition to x-ray micro-computed tomography [25, 26] and microscopic PIV measurements [41, 42], simulations using the lattice Boltzmann models reveal the pore scale information of high temporal resolution regarding interfacial areas and cluster sizes. In these models, the desired fluid and geometrical properties can be designed with powerful parallel computations and complex pore space geometry. So far, lattice Boltzmann models have been widely applied in the two-phase porous media flow simulation to address the problems of $p_c(s_w)$ curve [43, 44], $p_c(s_w, A_{nw})$ surface, $k_{r\sigma}(s_w)$ relation [27~29, 33~36], fluid distribution, and fluid displacement pattern [45~52]. The readers can refer to [53, 54] for a review of various multiphase lattice Boltzmann models, among which the Shan-Chen multi-component lattice Boltzmann model (SCMC-LBM) based on the interaction between particles [55~57] is rather efficient and versatile.

In the present work, the state-of-the-art SCMC-LBM model is used to conduct the simultaneous steady-state two-phase flow simulation based on two-dimensional porous media. Compared with previous studies [27~29, 33~40], this study focuses on exploring the role of film fluid and capillary pressure in the non-uniqueness of $k_{r\sigma}(s_w)$ relation, which has not been well understood so far. In the capillary force-dominated regime, the fluid distribution as well as the capillary pressure versus saturation curve subject to the influence of fluid and geometrical properties is characterized. How these factors are linked with the relative permeability versus saturation relation through the apparent effective permeability and the threshold pressure gradient is also investigated. Simulations were carried out including effects of fluid wettability, adhesive strength, pore size distribution and specific surface area, which are all important for fluid film formation and capillary pressure. The fluid-fluid, WP fluid-solid and NP fluid-solid interfacial areas serve as the fluid distribution descriptors. The following section will briefly describe the principle of SCMC-LBM model, setup of the fixed flow condition and the varying fluid and geometrical properties for the steady-state two-phase flow simulation as well as the procedure for post-processing simulation data. The SCMC-LBM simulation results will be discussed in Section 3, and conclusions drawn in the last section.

2. SCMC-LBM model

2.1. Model principle

Over the last two decades, the lattice Boltzmann models on the basis of mesoscopic kinetic theory [58] have been widely applied in simulating the two-phase porous media flow. Among them, the SCMC-LBM model based on the interaction between particles [55~57] is chosen in this study because of its efficiency and versatility. This model has also been well validated

against measured $p_c(s_w)$ curves [43, 44] and $k_{r\sigma}(s_w)$ relations [15, 34]. In the following, we briefly describe the basic model formulations.

The particle distribution function (f_i^σ) related to the ith discrete velocity direction at position ($\boldsymbol{x}$) at time (t) is assigned at each lattice node for each of the two fluid components, which evolves according to the lattice Boltzmann equation with the Bhatnagar-Gross-Krook (BGK) approximation as follows [58]

$$f_i^\sigma(\boldsymbol{x}+\boldsymbol{e}_i\Delta t, t+\Delta t) - f_i^\sigma(\boldsymbol{x},t) = -\frac{\Delta t}{\tau^\sigma}\left[f_i^\sigma(\boldsymbol{x},t) - f_i^{\sigma,eq}(\boldsymbol{x},t)\right], \quad (4)$$

where, $\boldsymbol{e}_i$ is the discrete velocity, Δt the time step, τ^σ the relaxation time and $f_i^{\sigma,eq}$ the Maxwell-Boltzmann equilibrium distribution function. Both of the two fluid components occupy each lattice node in the domain simultaneously, and the minor component can be considered as being dissolved within the major component. The left-hand side is a streaming process passing the particle distribution to the neighbouring nodes, while the right-hand side is a collision process partially relaxing the particle distribution to the equilibrium distribution. This discrete velocity model is commonly referred to as D_dQ_m model, where d and m are the number of dimensionalities and discrete velocities.

The macroscopic fluid density (ρ^σ) can be thought of as a series of direction-specific fluid densities, and the macroscopic flow velocity ($\boldsymbol{u}^\sigma$) is referred to as an average of the microscopic velocities weighted by the directional densities [58]

$$\rho^\sigma = \sum_{i=0}^{m-1} f_i^\sigma, \ \boldsymbol{u}^\sigma = \frac{1}{\rho^\sigma}\sum_{i=0}^{m-1} f_i^\sigma \boldsymbol{e}_i. \quad (5)$$

The equilibrium distribution function can be calculated by [58]

$$f_i^{\sigma,eq} = \rho^\sigma w_i\left[1 + \frac{\boldsymbol{e}_i\cdot\boldsymbol{u}^{\sigma,eq}}{c_s^2} + \frac{(\boldsymbol{e}_i\cdot\boldsymbol{u}^{\sigma,eq})^2}{2c_s^4} - \frac{\boldsymbol{u}^{\sigma,eq}\cdot\boldsymbol{u}^{\sigma,eq}}{2c_s^2}\right], \quad (6)$$

where, w_i are the weight coefficients, c_s the sound speed and $\boldsymbol{u}^{\sigma,eq}$ the equilibrium velocity. If the external force ($\boldsymbol{F}^\sigma$) is considered, the equilibrium velocity is expressed by [58]

$$\boldsymbol{u}^{\sigma,eq} = \boldsymbol{u}' + \frac{\tau^\sigma \boldsymbol{F}^\sigma}{\rho^\sigma}, \quad (7)$$

where, $\boldsymbol{u}'$ is the common velocity of the two fluid components. To obtain the equilibrium velocity, the density (ρ') and velocity ($\boldsymbol{u}'$) of the whole fluid are defined by [57]

$$\rho' = (\rho^\sigma + \rho^{\bar\sigma}), \ \boldsymbol{u}' = \sum_{\sigma\bar\sigma}\sum_{i=0}^{m}\frac{f_i^\sigma \boldsymbol{e}_i}{\tau^\sigma}\Big/\sum_{\sigma\bar\sigma}\frac{\rho^\sigma}{\tau^\sigma}. \quad (8)$$

The external force includes the body force $\boldsymbol{G}^\sigma = \rho^\sigma \boldsymbol{g}$, if specified, as well as the interaction forces ($\boldsymbol{F}_r^\sigma$) between fluid and fluid and ($\boldsymbol{F}_s^\sigma$) between fluid and solid, as follows [57],

$$\boldsymbol{F}^\sigma = \boldsymbol{G}^\sigma + \boldsymbol{F}_r^\sigma + \boldsymbol{F}_s^\sigma. \quad (9)$$

The repulsive interaction between σth and $\bar\sigma$th fluid component leading to phase separation and interface maintenance is realized by the inter-particle force, given by [56]

$$\boldsymbol{F}_r^\sigma(\boldsymbol{x},t) = -G_r\rho^\sigma(\boldsymbol{x},t)\sum_{i=1}^{m-1} w_i\rho^{\bar\sigma}(\boldsymbol{x}+\boldsymbol{e}_i\Delta t, t)\boldsymbol{e}_i, \quad (10)$$

where G_r is the repulsion parameter, which is positive and controls the strength of repulsive interaction. The repulsion strength determines the interfacial tension and the thickness of fluid-fluid interfacial layer. The phase separation for the uniformly mixing two fluid components can take place for $G_r\rho' > 1.0$ yielding the interfacial layer, while the interfacial layer thickness reaches convergence for $G_r\rho' > 1.6$ but the fluid compressibility begins to take

effect for $G_{\mathrm{r}}\rho' > 2.0$ [59]. The proper range for stable simulations is therefore $1.6 < G_{\mathrm{r}}\rho' < 2.0$ [59]. For the BGK-D_2Q_9 lattice Boltzmann model, the fluid pressure can be determined by [43]

$$p = c_{\mathrm{s}}^2(\rho' + G_{\mathrm{r}}\rho^{\sigma}\rho^{\bar{\sigma}}). \tag{11}$$

When the solid boundary is present, each fluid component may interact with the solid boundary independently. The adhesive interaction between σth fluid component and the solid particles can be achieved by the inter-particle force, as follows [58]

$$\boldsymbol{F}_{\mathrm{s}}^{\sigma}(\boldsymbol{x},t) = -G_{\mathrm{s}}^{\sigma}\rho^{\sigma}(\boldsymbol{x},t)\sum_{\mathrm{i}=1}^{\mathrm{m}-1} w_{\mathrm{i}} s(\boldsymbol{x}+\boldsymbol{e}_{\mathrm{i}}\Delta t,t)\boldsymbol{e}_{\mathrm{i}}, \tag{12}$$

where $s(\boldsymbol{x}+\boldsymbol{e}_i\Delta t,t)$ is an indicator function that equals 0 (1) for the σth fluid component (solid particles); and G_s^{σ} is the adhesion parameter, which is positive (negative) for the NP (WP) fluid [59, 60]. The difference in adhesion strengths for the WP and NP fluids determines the contact angle (θ). Two well-known approximations to the contact angle are expressed by

$$\cos(\theta) = \frac{G_{\mathrm{s}}^{\mathrm{n}} - G_{\mathrm{s}}^{\mathrm{w}}}{G_{\mathrm{r}}(\rho^{\mathrm{w}} - \rho^{\mathrm{n}})/2} \text{ [59]}, \quad \cos(\theta) = \frac{G_{\mathrm{s}}^{\mathrm{n}} - G_{\mathrm{s}}^{\mathrm{w}}}{G_{\mathrm{r}}} \text{ [60]}. \tag{13}$$

For the BGK-D_2Q_9 lattice Boltzmann model used in this study, the nine discrete velocities (a zero velocity and eight velocities pointing to the neighbouring nodes) and the weight coefficients are given as below [58]

$$[\boldsymbol{e}_0,\boldsymbol{e}_1,\boldsymbol{e}_2,\boldsymbol{e}_3,\boldsymbol{e}_4,\boldsymbol{e}_5,\boldsymbol{e}_6,\boldsymbol{e}_7,\boldsymbol{e}_8] = c\begin{bmatrix} 0 & 1 & 0 & -1 & 0 & 1 & -1 & -1 & 1 \\ 0 & 0 & 1 & 0 & -1 & 1 & 1 & -1 & -1 \end{bmatrix}, \tag{14}$$

$$[w_0,w_1,w_2,w_3,w_4,w_5,w_6,w_7,w_8] = \left[\frac{4}{9},\frac{1}{9},\frac{1}{9},\frac{1}{9},\frac{1}{9},\frac{1}{36},\frac{1}{36},\frac{1}{36},\frac{1}{36}\right]. \tag{15}$$

To recover the macroscopic Navier-Stokes equations from the BGK-D_2Q_9 lattice Boltzmann equation, the kinematic viscosity (ν^{σ}) related to the relaxation time and the sound speed related to the basic speed (c) should be formulated as [58]

$$\nu^{\sigma} = c_{\mathrm{s}}^2\left(\tau^{\sigma} - \frac{1}{2}\right)\Delta t, \tag{16}$$

$$c_{\mathrm{s}}^2 = \frac{c^2}{3}. \tag{17}$$

In order to circumvent the numerical difficulties [58], $\tau^{\sigma} = 1$ is the safest value far away from 0.5, and also the Mach number has to satisfy

$$M_{\mathrm{a}} = \frac{|\boldsymbol{u}^{\sigma}|_{\max}}{c_{\mathrm{s}}} \ll 1. \tag{18}$$

The basic speed is always taken as the ratio of lattice distance $\Delta x = 1$ lu to the time step $\Delta t = 1$ ts, *i.e.*, $c = \Delta x/\Delta t = 1$ lu/ts.

The simulation procedure during the time interval ($t^{\mathrm{n}-1} \to t^{\mathrm{n}}$) follows a few successive steps. First, $f_{\mathrm{i}}^{\sigma,\mathrm{eq},\mathrm{n}-1}$ are calculated from $\rho^{\sigma,\mathrm{n}-1}$ and $\boldsymbol{u}^{\sigma,\mathrm{n}-1}$ using Equation (6), and then $f_{\mathrm{i}}^{\sigma,\mathrm{n}-1}$ are collided following the rule of the BGK approximation in Equation (4). Second, $f_{\mathrm{i}}^{\sigma,\mathrm{n}-1}$ are streamed to the neighbouring nodes over $t^{\mathrm{n}-1} \to t^{\mathrm{n}}$ with the boundary condition implemented where needed. $f_{\mathrm{i}}^{\sigma,\mathrm{n}}$on the solid boundaries are obtained using the bounce-back boundary condition [60], such that $f_{\mathrm{i}}^{\sigma,\mathrm{n}} = f_{-\mathrm{i}}^{\sigma,\mathrm{n}-1}$ (where $-i$th represents the opposite direction to ith), and $f_i^{\sigma,\mathrm{n}}$ on the domain boundaries are treated as the periodic boundary condition [60] if the body force is specified as the driving force. Thirdly, $\rho^{\sigma,\mathrm{n}}$ and $\boldsymbol{u}^{\sigma,\mathrm{n}}$ are computed using $f_i^{\sigma,\mathrm{n}}$based on Equation (5). The simulation ends if the steady state criterion is reached, and $\rho^{\sigma,\mathrm{n}}$ and $\boldsymbol{u}^{\sigma,\mathrm{n}}$ are then stored, visualized and post-processed.

The discretization effect is an important aspect of the numerical solution in the SCMC-LBM simulations of real flow systems. *Pan et al.* [43] examined the minimum lattice resolution required for the simulation based on the three-dimensional packings of spheres with uniform size distributions, and found that the simulated intrinsic permeability and primary drainage $p_c(s_w)$ curve became essentially lattice resolution-independent if the mean pore throat radius was larger than 3 lattice units. The convergence of the numerical solution was also supported by good agreements with the experimental data [43]. *Sukop and Thorne* [60] proposed a similar rule of thumb that 4 or 5 lattice units were the minimum width of an open flow channel for converged solutions in the simulation of realistic hydrodynamics.

2.2. Model setup

In the fractional flow experiments [5~10, 37~40], the porous sample is mounted onto a flow cell with two series of syringe pumps that control the flux of individual fluids. The pressure drops measured by pressure sensors at the inlet and outlet of the cell are used for checking if the statistical equilibrium is reached. In similar manners, the steady-state two-phase flow simulation is conducted using the SCMC-LBM model based on two-dimensional porous media in this study. The units of distance, time and mass in the model are lu, ts and mu, respectively. Following the rule of conversion, *i.e.*, $1\ \mathrm{lu} = 1.0 \times 10^{-5}\mathrm{m}$, $1\ \mathrm{ts} = 5.0 \times 10^{-6}\mathrm{s}$ and $1\ \mathrm{mu} = 5.0 \times 10^{-13}\ \mathrm{kg}$, input properties and output variables of the model can be expressed in physical units in order to link mesoscopic simulations with engineering practices in real world.

2.2.1. Initial and boundary conditions

The present work focuses on the effect of varying fluid and geometrical properties on the macroscopic state variables. Thus all the simulations will be carried out under the fixed flow condition. Initially, the WP fluid is positioned in the centre of the upper and lower half regions, with the remaining region occupied by the NP fluid (Fig. 2). As such, the horizontal homogeneity of fluid distribution can be guaranteed when there is no external force to distribute the fluids horizontally. The width of WP fluid regions can be changed to adjust the overall WP fluid saturation in the whole simulation domain. The body force can be relatively easily implemented in the SCMC-LBM model. Thus the two-phase flow is driven by gravity vertically with the periodic boundary conditions [60] (Fig. 2). The outflowing fluids reenter the porous medium from the top inlet boundary periodically. In this way, capillary end effect can be accordingly avoided and the saturation keeps invariant during the flowing process. To ensure the capillary force-dominated regime, both fluids are subjected to the same gravity $g_\sigma = -6.0 \times 10^{-5}$, as expressed in terms of the magnitude of pressure gradient $[\nabla p] = 24$ KPa/m for convenience in interpretation. The flow simulations start with a zero velocity field.

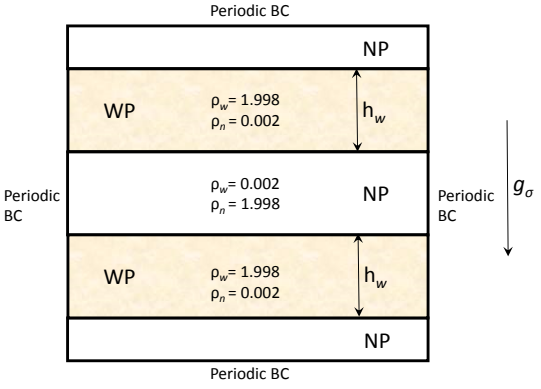

Fig. 2. Initial and boundary conditions in the SCMC-LBM model for the the steady-state two-phase flow simulation. The densities of WP and NP fluid components are specified in mu/lu^3.

2.2.2. Fluid and geometrical properties

In the capillary force-dominated regime, buoyancy effect and viscous coupling process are not significant [37, 38]. Thus the WP and NP fluids with equivalent densities and viscosities are adequate for approximating the oil-water or NAPL-water system with densities and viscosities of the same order of magnitude. In the SCMC-LBM model, each fluid phase consists of two fluid components. The density ratio of major component to minor one is set to be 999 (Fig. 2), and the physical density of each fluid phase is $\rho'_{\mathrm{w}}(\rho'_{\mathrm{w}}) = 1.0 \times 10^3$ kg/m^3. With the relaxation time 0.95 for stable numerical solutions [60], the physical dynamic viscosity of each fluid phase is taken as $\mu_{\mathrm{w}}(\mu_{\mathrm{n}}) = 3.0 \times 10^{-3}$ Pa•s. A segment of the randomly packed system with unequal grains is chosen to represent the REV of a two-dimensional porous medium. The lattice pixel number $M \bullet N = 800 \times 800$ is sufficient for a visualization of interfacial areas and fluid clusters. Thus dimension of the segment is 8.0mm × 8.0mm (Fig. 3b).

A benchmark case is established to illustrate the steady-state fluid distribution, interfacial areas, capillary pressure and relative permeability as presented in Section 3.1. The repulsive (adhesive) strength for fluid-fluid (fluid-solid) interaction in the model is taken to be $G_{\mathrm{r}}(G_{\mathrm{s}}) = 1.0$ (± 0.5). The fluid configuration in a tube at the capillary equilibrium (Fig. 3a) shows that the WP fluid has a strong wettability and a thin film forms near the solid wall. The resulted interfacial tension and contact angle are computed using the Laplace equation relating the pressure difference to the bubble curvature [12] and the fluid interface-based formula [59], respectively. An array of 300 unequal grains are initially deployed in contact with each other, in a way that the solid grains with a pre-defined radius distribution occupy the maximum volume within the given domain. In order to allow the two-phase fluid flow through the connected pore space, grain radii have to be shrunk while keeping the grain centre locations unchanged (Fig. 3b). The resulting minimum lattice pixel number of pore radius should obey the guidelines of the minimum pore throat radius required by the SCMC-LBM model for lattice resolution-independent simulation results [43, 60]. Using the coupled image processing algorithms [61], the throats and pores inside the REV can be separately detected, and the radii of realistic pores and grains are assumed to be equal to the radii of circular pores and grains with the same volume they occupy. Then specific grain surface area, average pore radius and porosity can be readily obtained. The distribution of pore sizes is fairly uniform (Fig. 5) in the sense that the pore uniformity coefficient $\frac{R_{60}}{R_{10}} \approx 1.5$ is less than 2 (R_{60} and R_{10} are the radii which 60% or 10% of the total pores are smaller than), and thus it can be considered as a less heterogeneous porous medium. The intrinsic permeability and tortuosity of packed grains are determined from the single phase flow simulation. The values of all fluid and geometrical properties are summarized in Table 1.

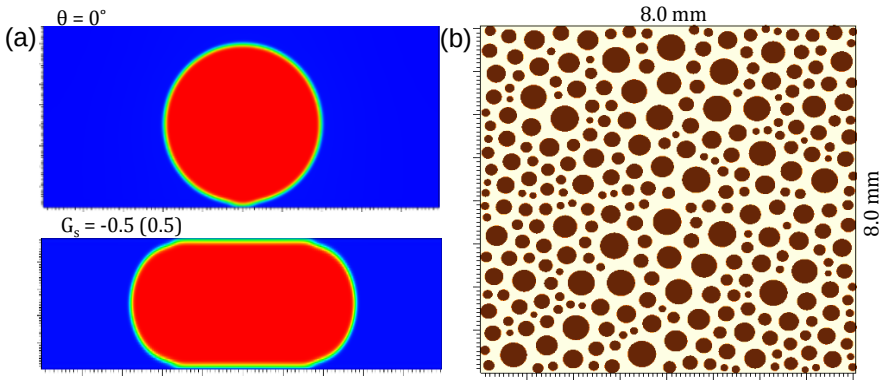

Fig. 3. Fluid with $G_r(G_s)$ = 1.0 ($\pm$0.5) in a tube at the capillary equilibrium (a), and porous medium with 300 unequal grains randomly packed (b) in the benchmark case. Blue, red and brown regions represent WP fluid, NP fluid and solid grains, respectively. Same as below.

Table 1. Properties of fluids and porous media in the simulation cases.

Properties		Values					Units
		Benchmark	Group 1		Group 2		
			$\theta = 55$	$\theta = 90$	$G_s = 1.5(5.5)$	$G_s = -2.5(-1.5)$	
Interfacial tension	γ	3.98	3.98	3.98	3.98	3.98	mN/m
Contact angle	θ	0	55	90	0	0	°
		Benchmark	Group 3		Group 4		
			PSD2	PSD3	Grain178	Grain452	
Porosity	ϕ	0.573	0.573	0.573	0.573	0.574	--
Average pore radius	R_{avg}	0.144	0.144	0.147	0.184	0.119	mm
Intrinsic permeability	k_{sat}	1.10	0.995	0.843	1.79	0.703	10^{-3} mm^2
Specific surface area	A_s	4.78	4.91	4.89	3.65	5.83	mm^{-1}
Tortuosity	Γ_y	1.15	1.19	1.24	1.15	1.15	--

To study the sensitivity of macroscopic state variables to changes of fluid properties under the fixed flow condition, the fluid property of interest in the benchmark case is varied with the geometrical property invariant, and vice versa. Four groups of test cases are designed, where the effects of wettability, adhesive strength, pore size distribution and specific surface area are examined separately. The benchmark case is referred to differently as $\theta = 0^\circ$, $G_s = -0.5(0.5)$, PSD1 and Grain 300 in the corresponding group. In group 1, with the constant interfacial tension, the repulsive (adhesive) strengths are specified by $G_r(G_s) = 1.0$ ($\pm$0.25) and 1.0 ($\pm$0) to produce the weak wettability and the neutral wettability (Fig. 4a). In group 2, the interfacial tension and the wettability are kept the same. The adhesive strengths $G_s = 1.5$ (5.5) generate a thin WP fluid film but the interactions become repulsive, while $G_s = -2.5$ (-1.5) results in a significant layer of WP fluid film (Fig. 4b). The following groups will adjust the number, size and position of grain array to achieve the desired characteristic. In group 3, the porous media have equal grain number and porosity but different pore size distributions (Fig. 5a). There are a larger fraction of macropores and fine pores for more heterogeneous PSD2 and PSD3 media than the benchmark medium. The average pore radii and the specific surface areas are almost same. In group 4, the porous media with the same porosity feature different specific surface areas (Fig. 5b). Grain178 and Grain452 media are filled with 178 and 452 unequal grains, respectively. The average pore radius for Grain178 (Grain452) media is larger (smaller) than that for the benchmark medium. The values of varied fluid and geometrical properties in each test case are listed in Table 1.

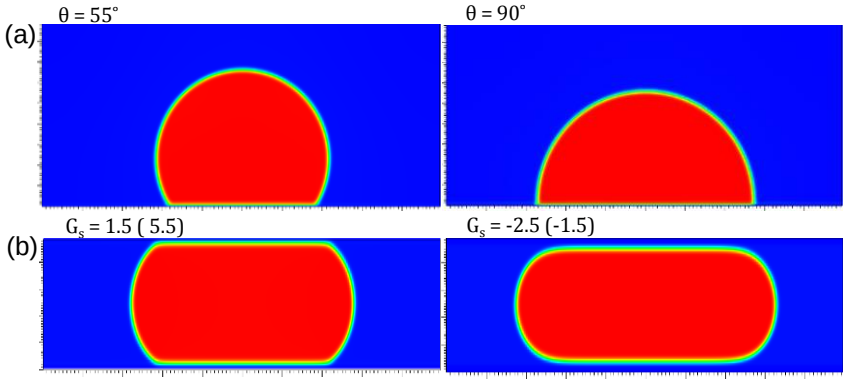

Fig. 4. Fluids with different contact angles (a) and adhesive strengths (b) in the test cases.

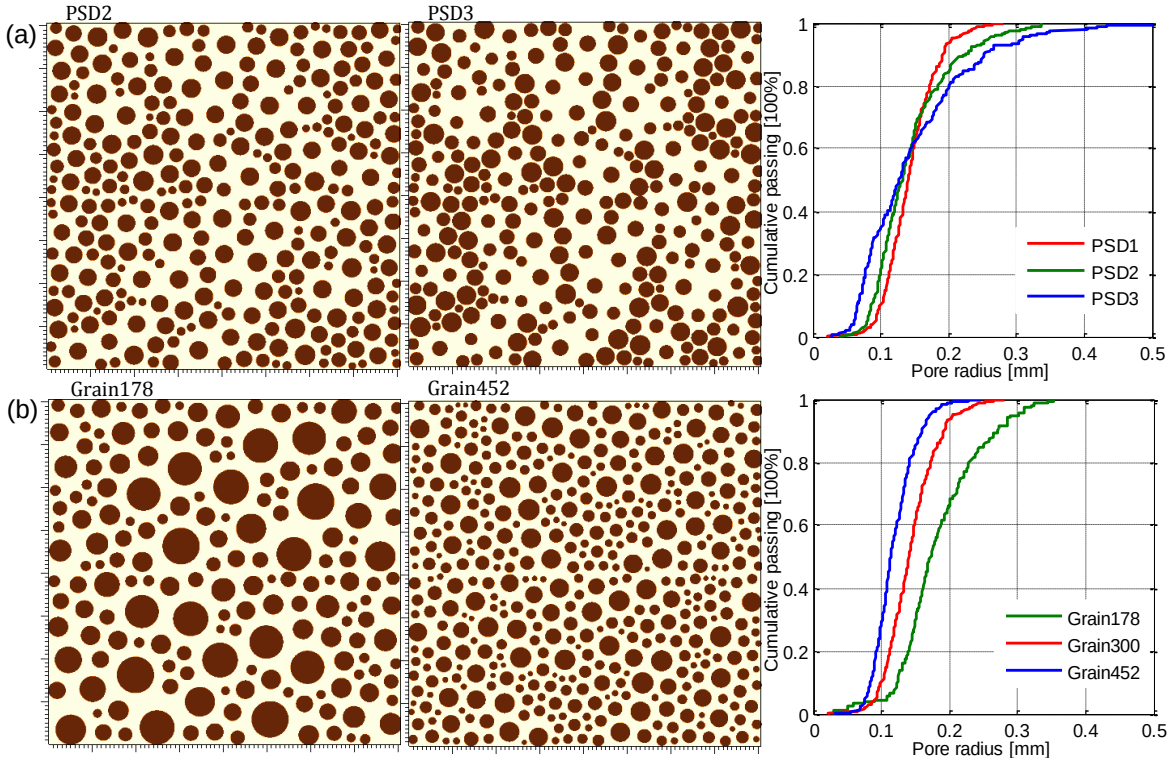

Fig. 5. Porous media with different pore size distributions (a) and specific surface areas (b) in the test cases. The cumulative passing percentage is defined as the percentage of pores in number which are smaller than a given radius.

2.3. Data post-processing

The SCMC-LBM model exports a series of density field and velocity field with time. Thus a post-processing procedure [11] is applied to transform the available outputs into the desired variables, *i.e.*, fluid saturation, interfacial areas, capillary pressure, relative permeability and capillary number.

2.3.1. Fluid saturation

To calculate the fluid saturation, in addition to the solid phase (SP) media, the WP and NP fluids need to be identified based on which kind of fluid particle dominates the lattice node. The simulated fluid-fluid interfacial area incurs spurious velocity [60] and thus has to be noted as the interphase (IP) fluid for special treatments in the calculation of fluid flux in Section 2.3.3. Each fluid phase can be identified individually based on density ρ_n of the NP fluid component at each lattice node and the empirical threshold densities (Table 2). For example, the lattice nodes with density of $0 < \rho_n < 0.2$ in the domain are considered as the WP fluid, the number of which is counted as N_w and the position of which is labelled as "10". Likewise, the NP fluid,

the SP media and the IP fluid can be identified with the number and position of corresponding lattice nodes.

Table 2. Density thresholds for identifying different phases (the density values are specified in mu/lu^3).

Phases	Thresholds	Lattices	Sign
WP	$0 < \rho_n < 0.2$	N_w	"10"
NP	$1.2 < \rho_n < 2.4$	N_n	"11"
SP	$\rho_n = 0$	N_s	"12"
IP	$0.2 \leq \rho_n \leq 1.2$	N_i	"13"

The IP fluid with a few lattices thickness occupies very slight fluid saturation, but it is still taken into account here and thus assigned to the WP and NP fluid saturations equally. Thus the saturation in terms of the WP fluid is expressed as the following

$$s_w = \frac{N_w + 0.5N_i}{M \bullet N - N_s}. \tag{19}$$

2.3.2. Interfacial areas and capillary pressure

The fluid-fluid and fluid-solid interfacial areas are used in this study to describe the fluid distribution. The boundary of WP fluid region is identified as the contour line with density of $\rho_n = 0.2$ using the *contour( )* function in MATLAB software. Then a number of WP fluid boundary segments with length L_{wi} can be extracted. The sum $\sum L_{wi}$ of disconnected boundaries can be used to represent the total surface area of WP fluid in the domain. Likewise, the boundaries of NP fluid and SP media can be identified as the contour line with density $\rho_n = 1.2$ and $\rho_n = 0$ individually, and the total surface area of NP fluid and SP media, $\sum L_{ni}$ and $\sum L_{si}$, can then be obtained. Subsequently, the fluid-fluid and fluid-solid interfacial areas defined in Equation (3) can be computed as follows [25, 26]

$$A_{nw} = \frac{\sum L_{ni} + \sum L_{wi} - \sum L_{si}}{2M \bullet N},\ A_{ws} = \frac{\sum L_{wi} - \sum L_{ni} + \sum L_{si}}{2M \bullet N},\ A_{ns} = \frac{\sum L_{ni} - \sum L_{wi} + \sum L_{si}}{2M \bullet N}. \tag{20}$$

The lattice nodes at the first layer of solid surface always have spurious density. Thus they are filtered out from WP and NP fluids when calculating the pressure of each fluid phase. The WP and NP fluid pressures are calculated by averaging fluid pressure p_{wi} and p_{ni} obtained from Equation (11) over the domain, and the capillary pressure defined in Equation (2) is then computed by

$$p_c = \frac{1}{N_n}\sum \frac{1}{3}(\rho_{wi} + \rho_{ni} + G_r\rho_{wi}\rho_{ni}) - \frac{1}{N_w}\sum \frac{1}{3}(\rho_{wi} + \rho_{ni} + G_r\rho_{wi}\rho_{ni}). \tag{21}$$

2.3.3. Relative permeability and capillary number

The spurious velocity occurs to the lattice nodes in the IP fluid as identified in Section 2.3.1 as well as at the first layer of solid surface. These nodes are thus excluded when calculating the flux. Since the gravity is imposed vertically as setup in Section 2.2.1, the fluid flux only in the y-axis are computed. The fluxes of WP and NP fluids are the average flow velocities u_{ywi} and u_{yni} as given by Equation (5) over the volume of the whole domain as follows

$$q_w = \frac{1}{M \bullet N}\sum(u_{ywi}),\ q_n = \frac{1}{M \bullet N}\sum(u_{yni}). \tag{22}$$

Then the relative permeabilities of WP and NP fluids defined in Equation (1) can be expressed based on the extended two-phase Darcy equation [12] as below

$$k_{rw} = \frac{q_w \nu_w / g_w}{k_{sat}},\ k_{rn} = \frac{q_n \nu_n / g_n}{k_{sat}}. \tag{23}$$

To describe the regime of steady-state two-phase flow, the capillary number (Ca) is computed based on the WP fluid flux as follows

$$Ca = \frac{1}{\phi s_{\mathrm{w}} \cos(\theta)} \frac{q_{\mathrm{w}} \mu_{\mathrm{w}}}{\gamma}. \quad (24)$$

The quantities calculated from Equations (19~24) fluctuate significantly with time because of the dynamic nature of the flow [5~10]. Thus a time-averaging procedure [11] is applied to avoid uncertainties in the simulation results. In this study, 2.0×10^5 time steps are sufficient to reach the statistical equilibrium at which the mean values of these quantities maintain quite stable.

3. Results and discussions

3.1. Benchmark case

At $s_{\mathrm{w}} = 0.102$ and 0.862, the major fluids are connected pathways, but the minor fluids are isolated in the form of bridges or ganglion (Fig. 6a). Meanwhile, at $s_{\mathrm{w}} = 0.478$, both of the WP and NP fluid packets are continuous in combination with several WP pendular rings and NP bubbles (Fig. 6a). Under the applied magnitude of pressure gradient, $[\nabla p] = 24$ KPa/m, the advancing fluid interface at $s_{\mathrm{w}} = 0.478$ occupies the whole pore throats, extends toward the pores perpendicular to the flow direction and even backward relative to the flow direction, and also elongates in the flow direction. These interfacial features indicate that capillary force dominates the two-phase fluid flow with $Ca = 0.00597$, where viscous coupling process is not significant. The flow diagram of *Huang et al.* [62] also shows that, with the given capillary number and the unit viscosity ratio, the flow pattern is close to the regime of capillary fingering. Each fluid occupies more solid surface as its saturation increases, but the fluid interface regulated by saturation of the minor fluid peaks at the intermediate saturation (Fig. 6b). Moreover, the WP fluid is more likely to contact the solid surface than the NP fluid for the specified strong wettability (Table 1), and thus $A_{\mathrm{ws}}(s_{\mathrm{w}})$ and $A_{\mathrm{ns}}(s_{\mathrm{w}})$ curves intersect at $s_{\mathrm{w}} < 0.5$ near which $A_{\mathrm{nw}}(s_{\mathrm{w}})$ curve attains the maximum (Fig. 6b). The WP pendular rings at $s_{\mathrm{w}} = 0.102$ and 0.478 tend to fill the narrow pore throats with the fluid interface that has larger curvature. The NP bubbles at $s_{\mathrm{w}} = 0.862$ and 0.478 prefer to stay in the large pore spaces with less curvy fluid interface, and the fluid interface of connected packets at $s_{\mathrm{w}} = 0.478$ elongating in the flow direction contributes slightly to capillary pressure. Therefore, the capillary pressure decreases with the increase in saturation (Fig. 6b). Furthermore, the $p_{\mathrm{c}}(s_{\mathrm{w}})$ curve is quite flat without a droopy tail near $s_{\mathrm{w}} \approx 1.0$ (Fig. 6b), which typically occurs in drainage. This is because the fluid saturation is independent of the applied magnitude of pressure gradient in the steady-state infiltration [11], while in drainage the NP fluid has to overcome the threshold pressure to enter the porous medium to reduce the WP fluid saturation [11]. Also, the $p_{\mathrm{c}}(s_{\mathrm{w}})$ curve is observed to be unique in the steady-state infiltration in the sense of no dependence on the saturation history, markedly different from the $p_{\mathrm{c}}(s_{\mathrm{w}})$ curve behaviors in drainage and imbibition [11].

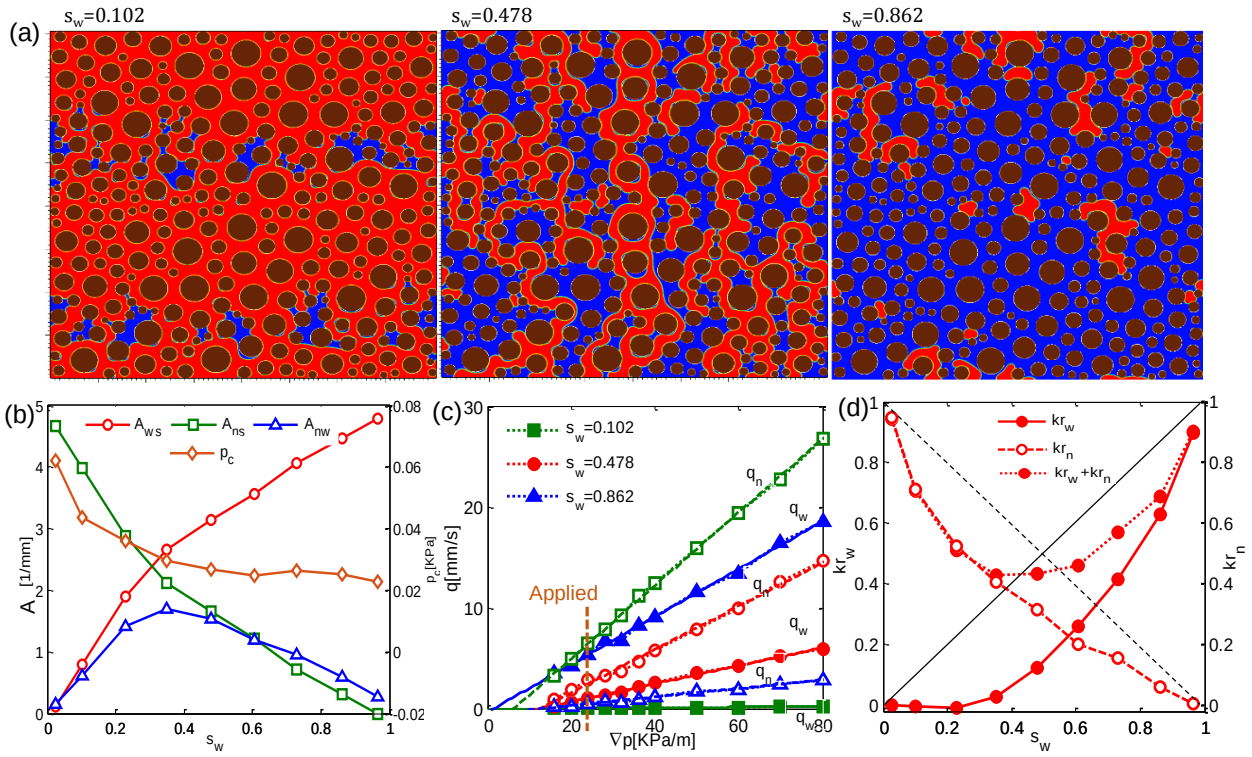

Fig. 6. Steady-state fluid distributions at $s_{\mathrm{w}} = 0.102, 0.478$ and 0.862 (a), $A_{\mathrm{ws}}(s_{\mathrm{w}})$, $A_{\mathrm{ns}}(s_{\mathrm{w}})$, $A_{\mathrm{nw}}(s_{\mathrm{w}})$ and $p_{\mathrm{c}}(s_{\mathrm{w}})$ curves (b), $q_{\mathrm{w}}(\nabla p)$ and $q_{\mathrm{n}}(\nabla p)$ lines at $s_{\mathrm{w}} = 0.102$, 0.478 and 0.862 (c), and $k_{\mathrm{rw}}(s_{\mathrm{w}})$, $k_{\mathrm{rn}}(s_{\mathrm{w}})$ and $(k_{\mathrm{rw}} + k_{\mathrm{rn}})(s_{\mathrm{w}})$ relations (d) in the benchmark case. In subfigure (c), the dotted symbols represent the original data of fluid flux, while the solid lines (for WP fluid) and the broken lines (for NP fluid) are the fitted lines. Same as below.

The data of fluid flux versus pressure gradient are evaluated using the linear regression approach, as performed in previous studies [30~32]. Within the given range of magnitude of pressure gradient, at $s_{\mathrm{w}} = 0.102, 0.478$ and 0.862, the flux of WP and NP fluids vary linearly with the pressure gradient (Fig. 6c), indicating laminar two-phase fluids flow; but the fitted lines have positive pressure gradient intercepts (Fig. 6c) below which the fluids cannot flow. As a result, $k_{\mathrm{r}\sigma}(s_{\mathrm{w}})$ relation shows a significant dependency on capillary number [11, 16~18]. Although it is unclear why there is a linear region for the data of fluid flux versus pressure gradient at the presence of film fluid and capillary pressure [19, 20], which are both intrinsic to the two-phase flow system, the linear relation has been widely observed [11] and implicitly assumed in the extended two-phase Darcy equation [12]. In this study, the slope and intercept of the fitted line of fluid flux versus pressure gradient are termed as apparent effective permeability (K_{σ}) and threshold pressure gradient ($[\nabla p]_{\mathrm{c}\sigma}$), respectively. If the effect of threshold pressure gradient is excluded, the computed effective permeabilities under the different magnitudes of pressure gradient collapse to apparent effective permeability [11]. By an analogy to the Kozeny-Carman equation [12], the apparent effective permeability is expected to be determined by saturation, tortuosity of flow path and fluid-solid interfacial area. The threshold pressure gradient is supposed to be caused by the film fluid induced by adhesive fluid-solid interaction and the capillary pressure including its constituents [19, 20]. On the other hand, when fluid and geometrical properties are varied, simultaneous K_{σ} decrease and $[\nabla \mathrm{p}]_{\mathrm{c}\sigma}$ increase result in the decrease in the effective permeability, while in the case of K_{σ} decrease but $[\nabla p]_{\mathrm{c}\sigma}$ decrease, how the effective permeability is affected depends on whether K_{σ} (including its constituents) or $[\nabla p]_{\mathrm{c}\sigma}$ (including its constituents) dominates the the two-phase flow process. Therefore, apparent effective permeability and threshold pressure gradient are able to link the fluid distribution as well as the capillary pressure as determined by fluid and geometrical properties with the relative permeability in a meaningful way.

Saturation is the dominated factor for K_σ, and also controls the magnitude of $[\nabla p]_{c\sigma}$. K_σ increases sharply but $[\nabla p]_{c\sigma}$ decreases rapidly with the increase in saturation of the corresponding fluid (Fig. 6c and Table 3). With the magnitude of pressure gradient invariant, the permeability of unsaturated porous media for a particular fluid is dominated by its amount. In small amount, the fluid can get easily entrapped in the narrow pore throats by adhesive and capillary forces; but, at the presence of more fluid in porous media, the redundant fraction of fluid occupying large pore space becomes easily mobile contributing to the total flux. It is interesting to note that, both fluids have positive threshold pressure gradients (Fig. 6c and Table 3). This indicates that the flows of not only the NP fluid but also the WP fluid are subjected to capillary resistance, which is different from the spontaneous imbibition case where the capillary force facilitates the WP fluid flow. This is due to the special flow pattern of the steady-state infiltration that features the competition between local drainage and local imbibition, and can be validated by the fact that the receding fluid interface is more curvy than the advancing fluid interface at $s_w = 0.102$ when the fluids flow towards the bottom outlet boundary (Fig. 6a). Also, the WP pendular rings at $s_w = 0.102$ have to be stagnant in the narrow pore throats, while the NP bubbles at $s_w = 0.862$ keep flowing through the porous media (Fig. 6a). It can be demonstrated by the magnitude of $[\nabla p]_{cw}$ at $s_w = 0.102$ (Table 3) which is close to the applied pressure gradient. In addition to larger capillary pressure ($s_w = 0.102$), the adhesive interaction may resist the WP fluid flow in the narrow pore throats.

Table 3. Values of K_σ, $[\nabla p]_{c\sigma}$ and $(k_{rw} + k_{rn})$ in the benchmark case and in the other test cases (at $s_w = 0.478$).

Cases		K_w	K_n	$[\nabla p]_{cw}$	$[\nabla p]_{cn}$	$(k_{rw} + k_{rn})$
Benchmark	$s_w = 0.102$	0.0041	0.362	21.15	6.30	0.705
	$s_w = 0.478$	0.0892	0.214	12.34	12.60	0.434
	$s_w = 0.862$	0.236	0.0424	1.45	12.90	0.688
Group 1	$\theta = 55$	0.0945	0.128	9.16	8.90	--
	$\theta = 90$	0.107	0.102	6.52	6.92	--
Group 2	$G_s =$ 1.5(5.5)	0.104	0.241	12.07	11.94	0.509
	$G_s =$ -2.5(-1.5)	0.0351	0.174	27.34	12.65	0.273
Group 3	PSD2	0.0693	0.191	16.67	9.27	--
	PSD3	0.0521	0.174	19.32	8.04	--
Group 4	Grain178	0.164	0.368	10.36	11.99	0.510
	Grain452	0.0559	0.112	15.91	14.70	0.256

As the saturation of each fluid increases, simultaneous K_σ increase and $[\nabla p]_{c\sigma}$ decrease lead to the nonlinear increase in the relative permeabilities (Fig. 6d). In addition, $k_{rw}(s_w)$ and $k_{rn}(s_w)$ relations intersect at $s_w > 0.5$ (Fig. 6d), showing that the WP relative permeability is smaller than the NP relative permeability at the same saturation of corresponding fluid; both $k_{rw}(s_w)$ and $k_{rn}(s_w)$ relations are concave (Fig. 6d) compared with the diagonal straight lines as expected for the zero interfacial tension, showing the loss of total permeability of the porous media when transmitting the two immiscible fluids. The irreducible saturation of the WP fluid as large as $s_w = 0.228$ is observed but there is no residual saturation of the NP fluid (Fig. 6d). These features are attributed to the fact that both fluids in the two-phase flow system are resisted by the same capillary force at any saturation, while the WP (NP) fluid is subjected to the strong (weak) adhesive interaction with the solid surface, as revealed by $K_w < K_n$ at $s_w = 0.478$ (Fig. 6c and Table 3). The value of $(k_{rw} + k_{rn})$ attains the minimum at $s_w = 0.350$ and 0.478 where the largest fluid-fluid interfacial area occurs producing the largest capillary resistance.

3.2. Effect of wettability

With the constant interfacial tension at $s_w = 0.478$ (Figs. 3a and 4a and Table 1), the fluid interface is rather curvy for the strong wettability (Fig. 6a). There exists a significant fraction of the WP fluid in the form of film fluid attaching to the back solid surface relative to the flow direction, and the WP fluid clusters are very discrete in terms of the fluid distribution. However, for the weak and neutral wettability, the fluid interface becomes quite flat (Fig. 7a). The WP fluid film starts to disappear and becomes connected. Thus, as the wettability weakens, the fluid interface has less fluid-fluid interfacial area, the WP fluid releases more solid surface for the NP fluid to occupy (Fig. 7b). For the neutral wettability, both $A_{ws}(s_w)$ and $A_{ns}(s_w)$ curves become straight lines and intercross at $s_w \approx 0.5$ (Fig. 7b), indicating that both fluids attach to the same area of solid surface at the equivalent saturation of each fluid; meanwhile, the capillary pressure drops across the whole range of saturation (Fig. 7b) as indicated by the Laplace equation [12] relating the capillary pressure to the wettability.

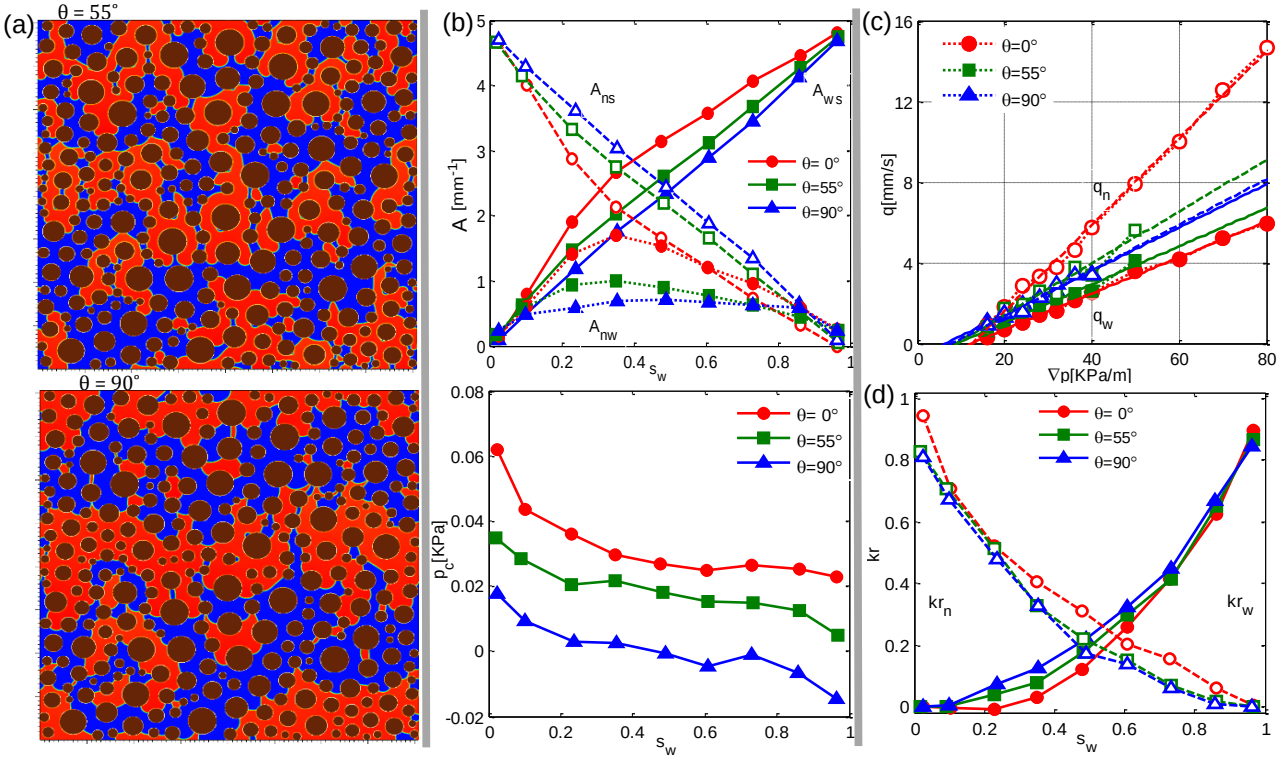

Fig. 7. Steady-state fluid distributions at $s_w = 0.478$ (a), $A_{ws}(s_w)$, $A_{ns}(s_w)$, $A_{nw}(s_w)$ and $p_c(s_w)$ curves (b), $q_w(\nabla p)$ and $q_n(\nabla p)$ lines at $s_w = 0.478$ (c), and $k_{rw}(s_w)$ and $k_{rn}(s_w)$ relations (d) for $\theta = 0°, 55°$ and $90°$.

For the WP (NP) fluid, the decrease (increase) in fluid-solid interfacial area results in significant K_w increase (K_n decrease). On the other hand, both the fluid-fluid interfacial area reduction and the capillary pressure decrease lead to a marked drop in $[\nabla p]_{c\sigma}$ of both fluids (Fig. 7c and Table 3), consistent with the conjecture [19, 20] that the threshold pressure gradient partly results from the capillary force. It is interesting to note that for the neutral wettability, the values of K_σ and $[\nabla p]_{c\sigma}$ of the two immiscible fluids are very close to each other (Table 3), in the sense that the fitted flux versus pressure gradient lines almost overlap each other (Fig. 7c). But the values of $[\nabla p]_{c\sigma}$ of the two immiscible fluids are not equal to zero (Table 3), as validated by the slight curvature of the fluid interface (Fig. 7a) contributing to the capillary resistance. Thus the contact angle is hysteretic with respect to whether the fluid interface is at the static equilibrium, receding or advancing [12]. Moreover, for all the given wettability, the difference between $[\nabla p]_{cw}$ and $[\nabla p]_{cn}$ is very slight (Table 3) showing the weak adhesive fluid-solid interactions because of the uniform distribution of pore size.

Both K_w increase and $[\nabla p]_{cw}$ decrease trigger a rise in the WP fluid relative permeability, but K_n decrease dominating $[\nabla p]_{cn}$ decrease causes a reduction in the NP fluid relative permeability (Fig. 7d), which is consistent with the results of previous studies [27, 28]. However, there is no much difference in $k_{rn}(s_w)$ relation for the weak and neutral wettability at $s_w < 0.350$ and $s_w > 0.729$ (Fig. 7d) as a result of the two opposing mechanisms. For the neutral wettability, $k_{rw}(s_w)$ and $k_{rn}(s_w)$ relations intercross at $s_w \approx 0.5$ and are both still concave (Fig. 7d), showing that the relative permeabilities of both fluids are very close to each other at the equivalent saturation of each fluid, and the slightly curvy fluid interface still contributes to the capillary resistance.

3.3. Effect of adhesive strength

When the interfacial tension and the wettability remain the same at $s_w = 0.478$ (Figs. 3a and 4b and Table 1), more WP fluid film is generated to coat the arbitrary side of the solid surface under stronger adhesive strength (Fig. 8a). As a result, the WP fluid is distributed very discretely and more fluid interface is produced (Fig. 8b). The WP fluid takes up more solid surface and the NP fluid has to be detached from more solid surface (Fig. 8b). For the adhesive strength $G_s = -2.5\ (-1.5)$, the WP fluid takes up almost 90% of the solid surface at $s_w = 0.478$, and the crossover of $A_{ws}(s_w)$ and $A_{ns}(s_w)$ curves appears at $s_w \approx 0.2$. In contrast, for the interaction strength $G_s = 1.5\ (5.5)$ which are both repulsive, the WP fluid occupies about 55% of the solid surface, and $A_{ws}(s_w)$ and $A_{ns}(s_w)$ curves intercross at $s_w \approx 0.45$ (Fig. 8b). Also, stronger adhesive strength induces greater capillary pressure across the whole range of saturation (Fig. 8b). In addition to capillary force, the adhesive fluid-solid interaction itself provides another source of capillary pressure [12], because of which the film fluid is formed with the WP fluid mobility reduced [21]. The viscosity of the WP fluid near the solid surface and the bulk fluid would be affected [22].

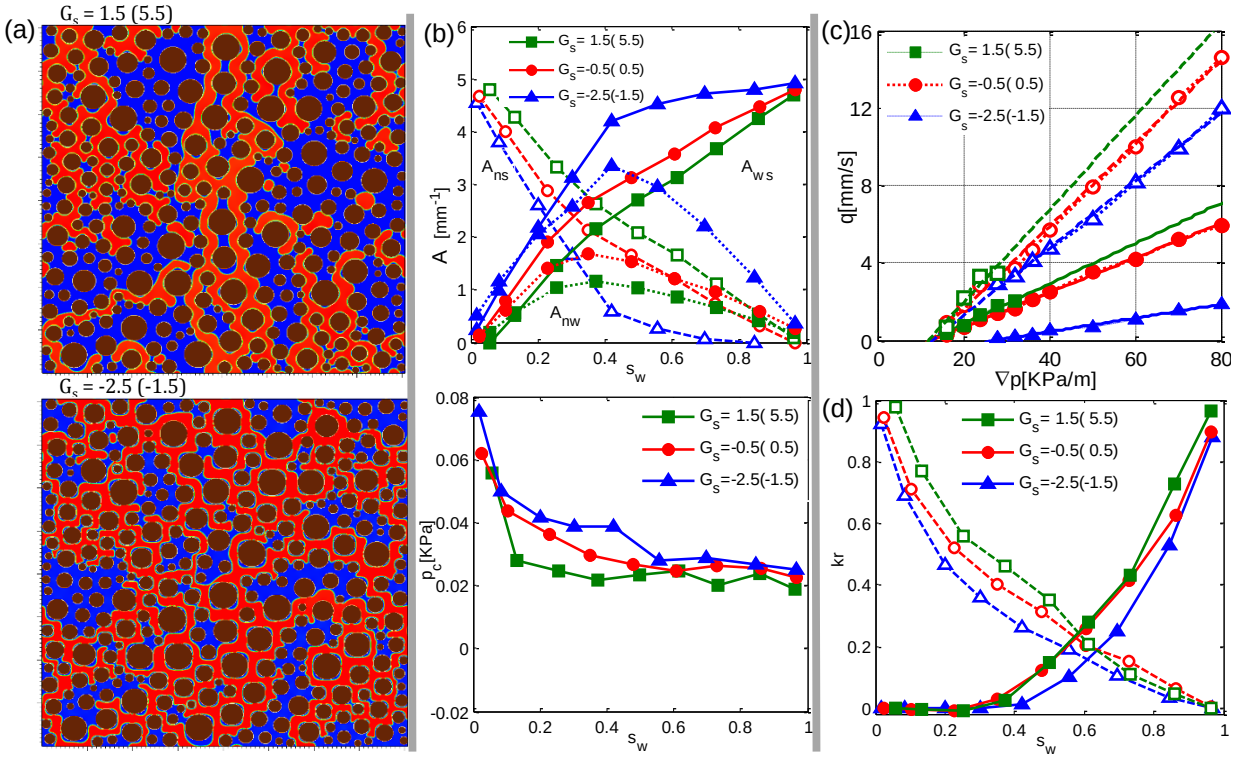

Fig. 8. Steady-state fluid distributions at $s_w = 0.478$ (a), $A_{ws}(s_w)$, $A_{ns}(s_w)$, $A_{nw}(s_w)$ and $p_c(s_w)$ curves (b), $q_w(\nabla p)$ and $q_n(\nabla p)$ lines at $s_w = 0.478$ (c), and $k_{rw}(s_w)$ and $k_{rn}(s_w)$ relations (d) for $G_s = 1.5(5.5)$, $-0.5(0.5)$ and $-2.5(-1.5)$.

Both the strong adhesive strength on the WP fluid-solid interfacial area and the increased WP fluid-solid interfacial area give rise to K_w decrease, while the strong adhesive strength on the NP fluid-solid interfacial area exceeding the decreased NP fluid-solid interfacial area brings about K_n decrease (Fig. 8c and Table 3). For the adhesive strength $G_s = -2.5\ (-1.5)$, K_w decrease is particularly significant (Fig. 8c and Table 3) as a result of the large increase in the solid surface covered by the WP fluid film and in the viscosity of the fluid near the solid surface. It can be seen that $K_w < K_n$ at the equivalent saturation of each fluid due to larger WP fluid-solid interfacial area and strengthened adhesive WP fluid-solid interaction. Greater capillary pressure and larger fluid interface almost do not affect $[\nabla p]_{cw}$ for $G_s = 1.5\ (5.5)$ and $-0.5\ (0.5)$, or $[\nabla p]_{cn}$ for all the given adhesive strengths (Fig. 8c and Table 3), indicating that the slight amount of WP fluid film does not dominate the WP fluid mobility compared with capillary force for $G_s = 1.5\ (5.5)$ and $-0.5\ (0.5)$. The capillary pressure induced by adhesive fluid-solid interaction and the fluid-fluid interfacial area resulting from the WP fluid film do not influence the mobility of NP fluid significantly. For the adhesive strength $G_s = -2.5\ (-1.5)$, a marked $[\nabla p]_{cw}$ increase occurs (Fig. 8c and Table 3) due to the large portion of WP fluid film with reduced mobility, consistent with the conjecture [19, 20] that the threshold pressure gradient partly results from the film fluid. Stronger adhesive WP fluid-solid interaction also leads to $[\nabla p]_{cw} > [\nabla p]_{cn}$.

The slight K_w decrease and the almost invariant $[\nabla p]_{cw}$ do not trigger a notable decrease in the WP relative permeability for $G_s = 1.5\ (5.5)$ and $-0.5\ (0.5)$ at $s_w < 0.729$, but the decrease in the WP relative permeability is significant for $G_s = -2.5\ (-1.5)$ at any saturation (Fig. 8d) as a result of significant K_w decrease and $[\nabla p]_{cw}$ increase. In addition, the irreducible WP fluid saturation in the form of film fluid is raised from 0.228 for $G_s = -0.5\ (0.5)$ to 0.420 for $G_s = -2.5\ (-1.5)$. On the other hand, K_n decrease and almost invariant $[\nabla p]_{cn}$ cause the decrease in the NP relative permeability for all the given adhesive strengths (Fig. 8d). The most loss in the total permeability of porous media at $s_w = 0.478$ occurs for $G_s = -2.5\ (-1.5)$ (Table 3).

3.4. Effect of pore size distribution

The specified porous media with equal porosities but different pore size distributions possess different intrinsic permeabilities because of different tortuosities of the flow path (Figs. 3b and 5a and Table 1). For the heterogeneous PSD3 medium with quite non-uniform pore sizes, the flow path is most tortuous (Table 1), and there are large fractions of macropores and fine pores (Fig. 5a). At $s_w = 0.478$, more WP fluid fills the narrow pore throats and more NP fluid occupies the large pore space making both fluids more connected (Fig. 9a). In the middle region of the PSD3 medium, the NP fluid forms a connected pathway (Region A) and another two large fluid clusters (Regions B and C), which take up the major fraction of NP fluid. Meanwhile, some macro-pores (Region D) are impossible for the NP fluid to enter because they are segregated by the fine pores relative to the flow direction. Thus a few small clusters as a minor part of the NP fluid are distributed discretely due to the initial distribution. All the WP fluid is divided into only two large fluid packets by the NP connected pathway. The improved fluid connectivity causes less fluid-fluid interfacial area, more solid surface contacted with the WP fluid, and less solid surface in touch with the NP fluid (Fig. 9b). The larger fraction of fine pores enhances the adhesive WP fluid-solid interaction [19, 20], and thus capillary pressure is larger at each saturation (Fig. 9b). Due to the heterogeneity of the PSD3 medium, it is easier for the WP fluid clusters to get trapped at some saturations. The immobile bubbles (with curvy interfacial area) contribute to larger capillary pressure, and thus $p_c(s_w)$

curve for the PSD3 medium experiences greater fluctuations (Fig. 9b) compared with the one for the PSD1 medium.

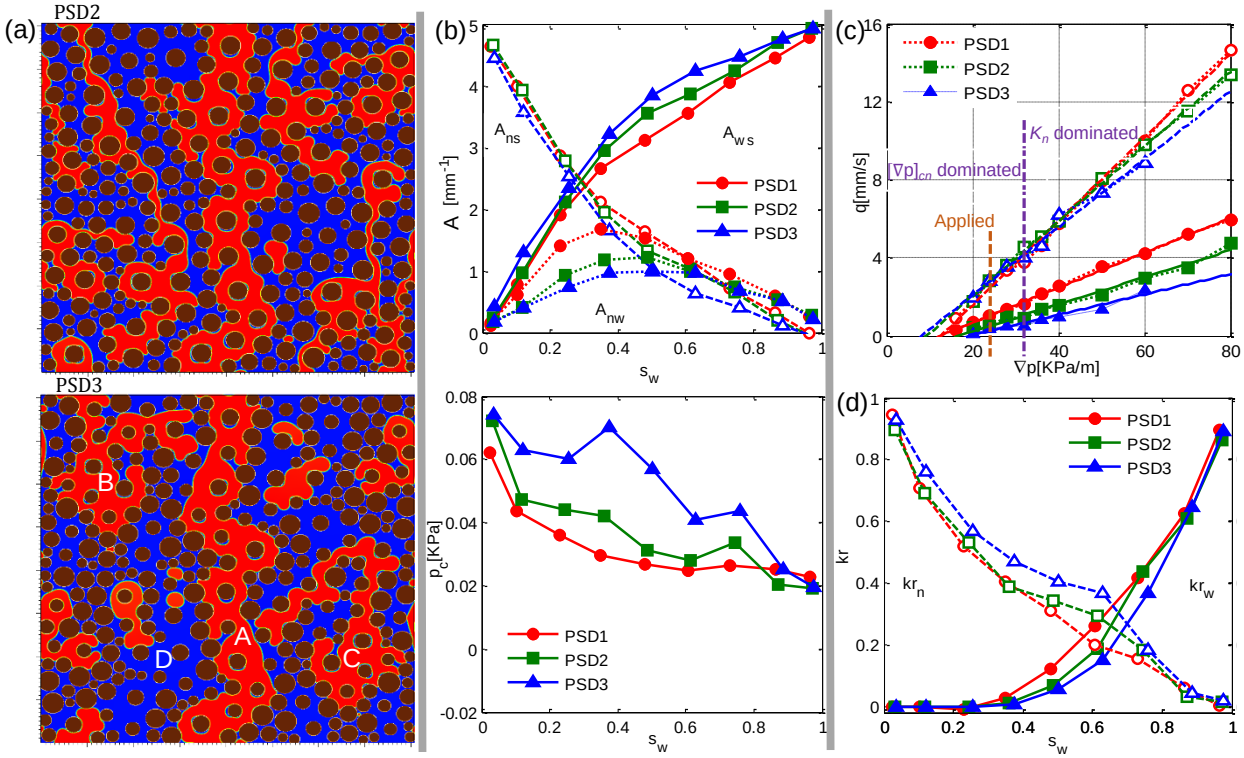

Fig. 9. Steady-state fluid distributions at $s_{\mathrm{w}} = 0.478$ (a), $A_{\mathrm{ws}}(s_{\mathrm{w}})$, $A_{\mathrm{ns}}(s_{\mathrm{w}})$, $A_{\mathrm{nw}}(s_{\mathrm{w}})$ and $p_{\mathrm{c}}(s_{\mathrm{w}})$ curves (b), $q_{\mathrm{w}}(\nabla \mathrm{p})$ and $q_{\mathrm{n}}(\nabla \mathrm{p})$ lines at $s_{\mathrm{w}} = 0.478$ (c), and $k_{\mathrm{rw}}(s_{\mathrm{w}})$ and $k_{\mathrm{rn}}(s_{\mathrm{w}})$ relations (d) for PSD1, PSD2 and PSD3.

Both the high tortuosity and the increased WP fluid-solid interfacial area lead to K_{w} decrease, but the high tortuosity overwhelming the decreased NP fluid-solid interfacial area is manifested in K_{n} decrease (Fig. 9c and Table 3). The enhanced adhesive WP fluid-solid interaction causes $[\nabla p]_{\mathrm{cw}}$ to increase, and the more connected NP fluid distribution renders $[\nabla p]_{\mathrm{cn}}$ to decrease (Fig. 9c and Table 3). These results show again that the adhesive interaction-induced capillary pressure does not affect the mobility of NP fluid. Also, for PSD2 and PSD3 media, $[\nabla p]_{\mathrm{cw}} > [\nabla p]_{\mathrm{cn}}$ is (Table 3) due to the adhesive WP fluid-solid interaction raised by the fine pores. It is interesting to note that K_{n} decrease and $[\nabla p]_{\mathrm{cn}}$ decrease result in a crossover of the fitted flux versus pressure gradient lines for the given porous media at $[\nabla p] \approx 32$ KPa/m (Fig. 9c), below which $[\nabla p]_{\mathrm{cn}}$ (capillary force) dominates the NP fluid flow and above which the NP fluid flow is dominated by K_{n} (viscous force).

Both K_{w} decrease and $[\nabla p]_{\mathrm{cw}}$ increase suggest a reduction in the WP relative permeability (Fig. 9d), while K_{n} decrease and $[\nabla p]_{\mathrm{cn}}$ decrease make the situation complicated. Under the applied pressure gradient $[\nabla p] = 24$ KPa/m, where the NP fluid flows in the capillary force-dominated regime, the NP effective permeability slightly increases as the heterogeneity of porous media strengthens (Fig. 9c). It should be also mentioned that the given porous media possess different intrinsic permeabilities, and thus the slight increase in the NP effective permeability is enlarged by the decreased intrinsic permeability in terms of the NP relative permeability (Fig. 9d and Table 1). The responses of the relative permeabilities of both fluids agree with the observations made in previous studies [33].

3.5. Effect of specific surface area

The given porous media with equivalent porosity feature different specific surface areas (Figs. 3b and 5b). For the Grain452 medium with larger specific surface area, the average pore radius

and the intrinsic permeability are both smaller (Figs. 3b and 5b and Table 1). The WP fluid preferring to stay in the fine pores becomes more continuous, resulting in less fluid-fluid interfacial area (Figs. 10a and 10b). However, for the Grain178 medium, the NP fluid tending to stay in the macro-pores may dominate the fluid connectivity. Thus there is no much difference in the fluid-fluid interfacial area between the Grain178 and Grain300 media (Figs. 6a, 10a and 10b). As the specific surface area increases, more solid surface becomes available for both fluids, and therefore, the WP fluid- and NP fluid- solid interfacial areas increase at the same saturation of each fluid (Fig. 10b). The capillary pressure is larger at any saturation (Fig. 10b) as indicated by the Laplace equation [12] relating the capillary pressure to the pore radius.

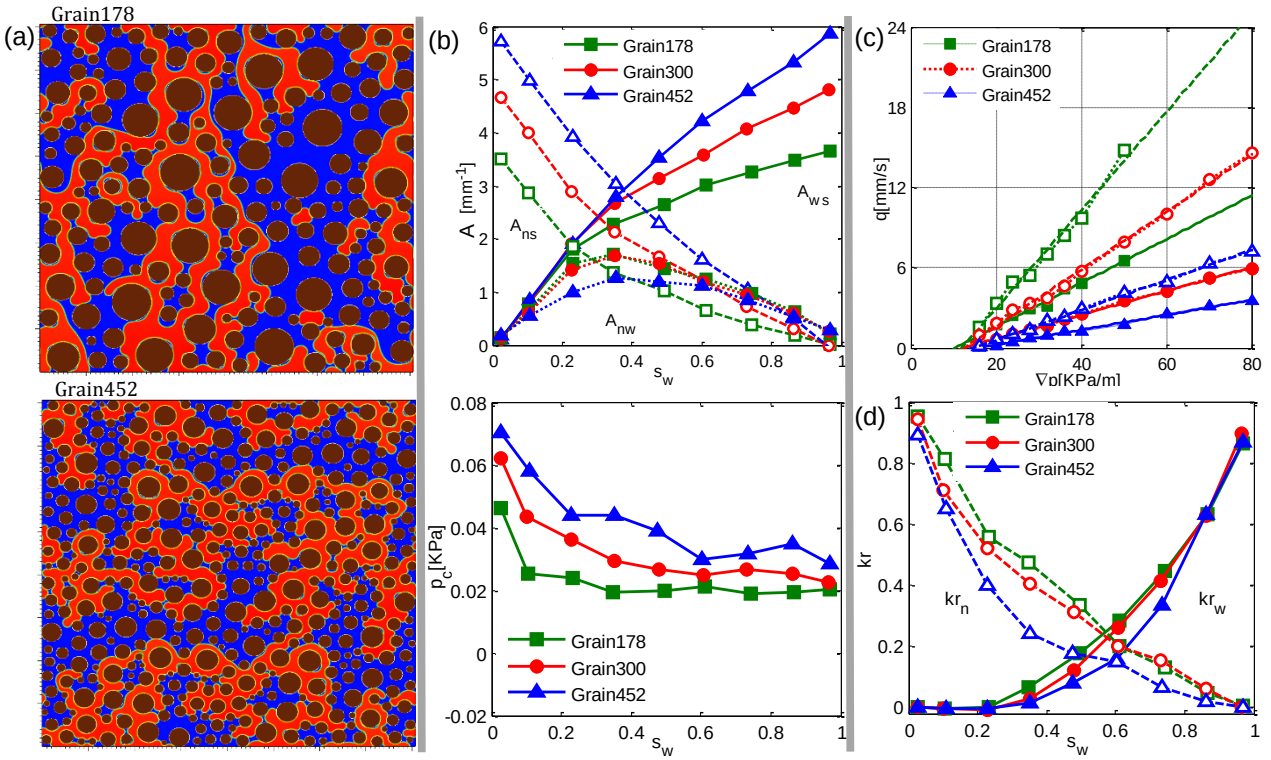

Fig. 10. Steady-state fluid distributions at $s_{\mathrm{w}} = 0.478$ (a), $A_{\mathrm{ws}}(s_{\mathrm{w}})$, $A_{\mathrm{ns}}(s_{\mathrm{w}})$, $A_{\mathrm{nw}}(s_{\mathrm{w}})$ and $p_{\mathrm{c}}(s_{\mathrm{w}})$ curves (b), $q_{\mathrm{w}}(\nabla \mathrm{p})$ and $q_{\mathrm{n}}(\nabla p)$ lines at $s_{\mathrm{w}} = 0.478$ (c), and $k_{\mathrm{rw}}(s_{\mathrm{w}})$ and $k_{\mathrm{rn}}(s_{\mathrm{w}})$ relations (d) for Grain178, Grain300 and Grain452.

For both fluids, the increase in fluid-solid interfacial area signifies K_{σ} decrease, and the capillary pressure increase dominating the fluid-fluid interfacial area decrease suggests a rise in $[\nabla p]_{\mathrm{c}\sigma}$ (Fig. 10c and Table 3). For the Grain452 medium, there is a slight trend of $[\nabla p]_{\mathrm{cw}} > [\nabla p]_{\mathrm{cn}}$ (Table 3) due to the enhanced adhesive WP fluid-solid interaction because of the smallest pore radius.

Both K_{σ} decrease and $[\nabla p]_{\mathrm{c}\sigma}$ increase indicate a reduction in the effective permeabilities of both fluids. It should be noted that as the specific surface area rise, the intrinsic permeability of porous media drops as well (Table 1). However, the relative permeabilities of both fluids still decrease significantly (Fig. 10d), showing the nonlinear response of the effective permeability to the specific surface area, which is different from the effect on the WP relative permeability observed in previous studies [34, 35]. This difference may reflect different conditions where the increased connectivity (as demonstrated by the decreased fluid-fluid interfacial area) or the increased capillary pressure (as a result of the narrowed pore radius) dominates the capillary resistance, and depends on the fraction of the effective fluid interface that contributes to the capillary resistance relative to the flow direction. The maximum loss in

660 the total permeability at $s_w = 0.478$ takes place for the Grain452 medium (Table 3) because of the enhanced adhesive WP fluid-solid interaction and the increased capillary resistance.

662 4. Conclusions

This study has been performed to explore the roles of the film fluid as a result of the adhesive 664 fluid-solid interaction and the capillary pressure [19, 20] in the non-uniqueness of $k_{r\sigma}(s_w)$ relation. It is found that the apparent effective permeability and the threshold pressure 666 gradient can be used to link the fluid distribution as well as the capillary pressure as determined by fluid and geometrical properties with the relative permeability meaningfully. 668 The sensitivity of fluid distribution and constitutive relationships to wettability, adhesive strength, pore size distribution and specific surface area is tested using the state-of-the-art 670 SCMC-LBM model on two-dimensional simultaneous flow cell. Key findings are summarized as the following.

672 (1) Each fluid occupies more solid surface as the saturation and the available solid surface increase, and the WP fluid tends to take up more solid surface than the NP fluid at the same 674 saturation of each fluid. Once the thin WP fluid film is formed, it can coat the solid surface with a slight saturation, which repels the NP fluid. In the heterogeneous porous media, the WP (NP) 676 fluid filling the fine pores (macropores) seizes more (less) solid surface.

(2) The fluid interface regulated by the saturation of the minor fluid peaks at the intermediate 678 saturation. In the form of film fluid, the WP fluid is very discretely distributed resulting in the significantly increased fluid-fluid interfacial area. In the heterogeneous porous media, the WP 680 (NP) fluid tending to fill the narrow (large) pore space makes both fluids more connected. On the other hand, for the small (large) average pore radius, the WP (NP) fluid becomes more 682 continuous in the less heterogeneous porous media. The fluid-fluid interfacial area is a good parameter for describing the fluid connectivity.

684 (3) The capillary pressure decreases with the increase in saturation, and $p_c(s_w)$ curve is relatively flat without a droopy tail at $s_w \approx 1.0$ in the steady-state infiltration. The effect of 686 wettability and average pore radius on the capillary pressure follows the indications by the Laplace equation [12]. In addition to the capillary force, the adhesive fluid-solid interaction 688 provides another source of capillary pressure, which can be enhanced by the large adhesive strength and the fine pores in the heterogeneous porous media.

690 (4) The apparent effective permeability of each fluid increases with the increase in its saturation, but decreases with the increase in tortuosity of flow path and fluid-solid interfacial 692 area, which is consistent with the Kozeny-Carman equation [12]. Also, it maintains a negative correlation with the adhesive strength on the fluid-solid interfacial area. At the equivalent 694 saturation, K_w is smaller than K_n.

(5) The threshold pressure gradient is dominated by the saturation of each fluid. Small amount 696 of one fluid gets easily entrapped in the narrow pore space. $[\nabla p]_{cw}$ originates from the film fluid with the reduced mobility and the capillary resistance as well in the steady-state 698 infiltration. On the other hand, $[\nabla p]_{cn}$ is due to the capillary resistance, but the adhesive interaction-induced capillary pressure does not affect the mobility of NP fluid. At the same 700 saturation, $[\nabla p]_{cw}$ can exceed $[\nabla p]_{cn}$ when the film fluid effect is significant for the strong adhesive strength or for the heterogeneous porous media with fine pores.

702 (6) Simultaneous K_σ decrease and $[\nabla p]_{c\sigma}$ increase result in the decrease in the effective permeability, while in the case of K_σ decrease but $[\nabla p]_{c\sigma}$ decrease, how the effective

permeability varies depends on whether K_σ or $[\nabla p]_{c\sigma}$ dominates the two-phase flow process under the applied pressure gradient. K_σ ($[\nabla p]_{c\sigma}$) is expected to play a dominant role under the large (small) applied pressure gradient. The effect on the effective permeability may be enlarged by decreased intrinsic permeability in terms of the relative permeability. The effective permeability is nonlinearly correlated with saturation and specific solid surface.

The two-phase flow system in the steady-state infiltration is a coupled thermo-hydrodynamic process, as revealed by the effect of film fluid and capillary pressure on the relative permeabilities of both fluids. The strong wettability of WP fluid and the increased adhesive WP fluid-solid strength reflect the introduction of more surface energy into the flow system, and thus both the capillary pressure and the fluid-fluid interfacial area rise at all saturations. Meanwhile, when the geometrical property is varied, the capillary pressure responds reversely relative to the fluid-fluid interfacial area at each saturation, implying the conservation of surface energy in the flow system. The findings from this study, elucidating the roles of film fluid and capillary pressure in the two-phase flow system, have implications for improving the macroscopic flow equation through balance of force for the steady-state infiltration.

Acknowledgments

The primary data of grain sizes and packing are downloaded from the Packomania webpage [63]. All the simulations were executed using the Mechsys open source library [64] and the Goliath high performance computing cluster of the University of Queensland. The first author would like to acknowledge the support of International Postgraduate Research Scholarship (IPRS) and University of Queensland Centennial Scholarship (UQCent). The authors also thank the three anonymous reviewers for their thorough reviews and constructive comments.

References

[1] Oostrom, M., Lenhard, R. J., 1998. Comparison of relative permeability-saturation-pressure parametric models for infiltration and redistribution of a light non-aqueous-phase liquid in sandy porous media. *Adv Water Resour*, *21*(2), 145–157. https://doi.org/10.1016/S0309-1708(96)00038-3.

[2] Fagerlund, F. F., Niemi, A., Oden M., 2006. Comparison of relative permeability–fluid saturation–capillary pressure relations in the modelling of non-aqueous phase liquid infiltration in variably saturated, layered media. *Adv Water Resour*, *29*(11), 1705–1730. https://doi.org/10.1016/j.advwatres.2005.12.007.

[3] Liu, P., Zhang, X., 2015. Enhanced oil recovery by CO_2–CH_4 flooding in low permeability and rhythmic hydrocarbon reservoir. *Int J Hydrogen Energ*, *40*(37), 12849–12853. https://doi.org/10.1016/j.ijhydene.2015. 07.013.

[4] Yu, W., Lashgari, H. R., Wu, K., Sepehrnoori, K., 2015. CO_2 injection for enhanced oil recovery in Bakken tight oil reservoirs. *Fuel*, *159*, 354–363. https://doi.org/10.1016/j.fuel.2015.06.092.

[5] Avraam, D. G., Payatakes, A. C., 1995a. Flow regimes and relative permeabilities during steady-state two-phase flow in porous media. *J Fluid Mech*, *293*, 207–236. https://doi.org/10.1017/S0022112095001698.

[6] Avraam, D. G., Payatakes, A. C., 1995b. Generalized Relative Permeability Coefficients during Steady-State Two-Phase Flow in Porous Media , and Correlation with the Flow Mechanisms. *Transp Porous Media*, *20*, 135–168. https://doi.org/10.1007/BF00616928.

[7] Avraam, D. G., Payatakes, A. C., 1999. Flow mechanisms, relative permeabilities, and coupling effects in steady-state two-phase flow through porous media. The case of strong wettability. *Ind Eng Chem Res*, *38*(3), 778–786. https://doi.org/10.1021/ie980404o.

[8] Tallakstad, K. T., Løvoll, G., Knudsen, H. A., Ramstad, T., et al., 2009. Steady-state, simultaneous two-phase flow in porous media: An experimental study. *Phys Rev E*, *80*(3), 1–13. https://doi.org/10.1103/PhysRevE.80.036308.

[9] Tallakstad, K. T., Knudsen, H. A., Ramstad, T., Løvoll, G., et al., 2009. Steady-state two-phase flow in porous media: Statistics and transport properties. *Phys Rev Lett*, *102*(7), 100–103. https://doi.org/10.1103/PhysRevLett.102.074502.

[10] Erpelding, M., Sinha, S., Tallakstad, K. T., Hansen, A., et al., 2013. History independence of steady state in simultaneous two-phase flow through two-dimensional porous media. *Phys Rev E*, *88*(5), 1–12. https://doi.org/10.1103/PhysRevE.88.053004.

[11] Li, Z., Galindo-Torres, S. A., Yan, G., Scheuermann, A., Li, L., 2017. Numerical simulation of simultaneous steady-state two-phase flow dynamics using the lattice Boltzmann model: interfacial area, capillary pressure and relative permeability. *Submitted.*

[12] Bear, J., Cheng, A. H.-D., 2010. *Modeling Groundwater Flow and Contaminant Transport*. New York: Springer Dordrecht Heidelberg London.

[13] Dana, E., Skoczylas, F., 2002. Experimental study of two-phase flow in three sandstones. I. Measuring relative permeabilities during two-phase steady-state experiments. *Int J Multiphase Flow*, *28*(11), 1719–1736. https://doi.org/10.1016/S0301-9322(02)00090-3.

[14] Tsakiroglou, C. D., Avraam, D. G., Payatakes, A. C., 2007. Transient and steady-state relative permeabilities from two-phase flow experiments in planar pore networks. *Adv Water Resour*, *30*(9), 1981–1992. https://doi.org/10.1016/j.advwatres.2007.04.002.

[15] Ramstad, T., Idowu, N., Nardi, C., Øren, P.-E., 2012. Relative Permeability Calculations from Two-Phase Flow Simulations Directly on Digital Images of Porous Rocks. *Transp Porous Media*, *94*(2), 487–504. https://doi.org/10.1007/s11242-011-9877-8.

[16] Constantinides, G. N., Payatakes, A. C., 1996. Network simulation of steady-state two-phase flow in consolidated porous media. *AIChE J*, *42*(2), 369–382. https://doi.org/10.1002/aic.690420207.

[17] Henderson, G. D., Danesh, A., Tehrani, D. H., Peden, J. M., 1997. The effect of velocity and interfacial tension on relative permeability of gas condensate fluids in the wellbore region. *J Pet Sci Eng*, *17*(3-4), 265–273. https://doi.org/10.1016/S0920-4105(96)00048-4.

[18] Huang, H., Lu, X., 2009. Relative permeabilities and coupling effects in steady-state gas-liquid flow in porous media: A lattice Boltzmann study. *Phys Fluids*, *21*(9), 092104. https://doi.org/10.1063/1.3225144.

[19] Hao, F., Cheng, L. S., Hassan, O., Hou, J., et al., 2008. Threshold Pressure Gradient in Ultra-low Permeability Reservoirs. *Pet Sci Technol*, 26(9), 1024–1035. https://doi.org/10.1080/10916460701675033.

[20] Dou, H., Ma, S., Zou, C., Yao, S., 2014. Threshold pressure gradient of fluid flow through multi-porous media in low and extra-low permeability reservoirs. *Sci Earth China Sci*, *57*(11), 2808–2818. https://doi.org/10.1007/s11430-014-4933-1.

[21] Longmuir, G., 2004. Pre-Darcy Flow : A Missing Piece of the Improved Oil Recovery Puzzle? *2004 SPE/DOE Fourteenth Symposium on Improved Oil Recovery*, 1–14.

[22] Benzi, R., Biferale, L., Sbragaglia, M., Succi, S., Toschi, F., 2006. Mesoscopic two-phase model for describing apparent slip in micro-channel flows. *Europhys Lett*, *74*(4), 651–657. https://doi.org/10.1209/epl/i2006-10022-0.

[23] Hassanizadeh, S. M., Gray, W. G., 1993a. Toward an improved description of the physics of two-phase flow. *Adv Water Resour*, *16*(1), 53–67. https://doi.org/10.1016/0309-1708(93)90029-F.

[24] Hassanizadeh, S. M., Gray, W. G., 1993b. Thermodynamic basis of capillary pressure in porous media. *Water Resour Res*, *29*(10), 3389–3405. https://doi.org/10.1029/93WR01495.

[25] Chen, D., Pyrak-Nolte, L. J., Griffin, J., Giordano, N. J., 2007. Measurement of interfacial area per volume for drainage and imbibition. *Water Resour Res*, *43*(12), 1–6. https://doi.org/10.1029/2007WR006021.

[26] Porter, M. L., Wildenschild, D., Grant, G., Gerhard, J. I., 2010. Measurement and prediction of the relationship between capillary pressure, saturation, and interfacial area in a NAPL-water-glass bead system. *Water Resour Res*, *46*(8), 1–10. https://doi.org/10.1029/2009WR007786.

[27] Li, H., Pan, C., Miller, C. T., 2005. Pore-scale investigation of viscous coupling effects for two-phase flow in porous media. *Phys Rev E*, *026705*, 1–14. https://doi.org/1539-3755/2005/72(2)/026705(14).

[28] Hao, L., Cheng, P., 2010. Pore-scale simulations on relative permeabilities of porous media by lattice Boltzmann method. *Int J Heat Mass Transf*, *53*(9-10), 1908–1913. https://doi.org/10.1016/j.ijheatmasstransfer.2009.12.066.

[29] Landry, C. J., Karpyn, Z. T., Ayala, O., 2014. Relative permeability of homogenous-wet and mixed-wet porous media as determined by pore-scale lattice Boltzmann modeling. *Water Resour Res*, *50*(5), 3672–3689. https://doi.org/10.1002/2013WR015148.

[30] Swartzendruber, D., 1962. Non-Darcy flow behavior in liquid-saturated porous media. *J Geophys Res*, *67*(13), 5205–5213. https://doi.org/10.1029/JZ067i013p05205.

[31] Miller, R. J., Low, P. F., 1963. Threshold Gradient for Water Flow in Clay Systems. *Soil Sci Soc Am J, 27*, 605–609.

[32] Prada, A., Civan, F., 1999. Modification of Darcy's law for the threshold pressure gradien. *J Pet Sci Eng*, *22*, 237–240.
[33] Dou, Z., Zhou, Z.-F., 2013. Numerical study of non-uniqueness of the factors influencing relative permeability in heterogeneous porous media by lattice Boltzmann method. *Int J Heat Fluid Flow*, *42*, 23–32. https://doi.org/10.1016/j.ijheatfluidflow.2013.01.020.
[34] Ghassemi, A., Pak, A., 2011. Numerical study of factors influencing relative permeabilities of two immiscible fluids flowing through porous media using lattice Boltzmann method. *J Pet Sci Eng*, *77*, 135–145. https://doi.org/10.1016/j.petrol.2011.02.007.
[35] Gao, C., Xu, R. N., Jiang, P. X., 2015. Pore-scale numerical investigations of fluid flow in porous media using lattice Boltzmann method. *Int J Numer Methods Fluids*, *25*(8), 1957–1977. https://doi.org/10.1108/HFF-07-2014-0202.
[36] Zhang, D., Papadikis, K., Gu, S., 2016. A lattice Boltzmann study on the impact of the geometrical properties of porous media on the steady state relative permeabilities on two-phase immiscible flows. *Adv Water Resour*, *95*, 61–79. https://doi.org/10.1016/j.advwatres.2015.12.015.
[37] Valavanides, M. S., Constantinides, G. N., Payatakes, A. C., 1998. Mechanistic Model of Steady-State Two-Phase Flow in Porous Media Based on Ganglion Dynamics. *Transp Porous Media*, *30*(3), 267–299. https://doi.org/10.1023/A:1006558121674.
[38] Valavanides, M. S., Payatakes, A. C., 2001. True-to-mechanism model of steady-state two-phase flow in porous media, using decomposition into prototype flows. *Adv Water Resour*, *24*(3-4), 385–407. https://doi.org/10.1016/S0309-1708(00)00063-4.
[39] Yiotis, A. G., Talon, L., Salin, D., 2013. Blob population dynamics during immiscible two-phase flows in reconstructed porous media. *Phys Rev E*, *87*(3), 1–12. https://doi.org/10.1103/PhysRevE.87.033001.
[40] Armstrong, R. T., McClure, J. E., Berrill, M. A., Rucker, M., et al., 2016. Beyond Darcy's law: The role of phase topology and ganglion dynamics for two-fluid flow. *Phys Rev E*, *94*(4), 1–10. https://doi.org/10.1103/PhysRevE.94.043113.
[41] Kazemifar, F., Blois, G., Kyritsis, D. C., Christensen, K. T., 2016. Quantifying the flow dynamics of supercritical CO_2–water displacement in a 2D porous micromodel using fluorescent microscopy and microscopic PIV. *Adv Water Resour*, *95*, 352–368. https://doi.org/10.1016/j.advwatres.2015.05.011.
[42] Li, Y., Kazemifar, F., Blois, G., Christensen, K. T., 2017. Micro-PIV measurements of multiphase flow of water and liquid CO_2 in 2-D heterogeneous porous micromodels, *Water Resour Res*, *53*, 6178–6196. https://doi.org/10.1002/2017WR020850.
[43] Pan, C. X., Hilpert, M., Miller, C. T., 2004. Lattice-Boltzmann simulation of two-phase flow in porous media. *Water Resour Res*, *40*(2), W01501. https://doi.org/10.1029/2003WR002120.
[44] Schaap, M., Porter, M., Christensen, B. S. B., Wildenschild, D., 2007. Comparison of pressure-saturation characteristics derived from computed tomography and lattice Boltzmann simulations. *Water Resour Res*, *43*, W12S06. https://doi.org/10.1029/2006WR005730.
[45] Liu, H., Valocchi, A. J., Werth, C., Kang, Q., Oostrom, M., 2014. Pore-scale simulation of liquid CO_2 displacement of water using a two-phase lattice Boltzmann model. *Adv Water Resour*, *73*, 144–158. https://doi.org/10.1016/j.advwatres.2014.07.010.
[46] Liu, H., Zhang, Y., Valocchi, A. J., 2015. Lattice Boltzmann simulation of immiscible fluid displacement in porous media: Homogeneous versus heterogeneous pore network. *Phys Fluids*, *27*(5), 052103. https://doi.org/10.1063/ 1.4921611.
[47] Tsuji, T., Jiang, F., Christensen, K. T., 2016. Characterization of immiscible fluid displacement processes with various capillary numbers and viscosity ratios in 3D natural sandstone. *Adv Water Resour*, *95*, 3–15. https://doi.org/10.1016/j.advwatres.2016.03.005.
[48] Xu, Z., Liu, H., Valocchi, A. J., 2017. Lattice Boltzmann simulation of immiscible two-phase flow with capillary valve effect in porous media. *Water Resour Res*, *53*(5), 3770–3790. https://doi.org/10.1002/2017WR020373.
[49] Zhang, C., Oostrom, M., Wietsma, T. W., et al., 2011. Influence of viscous and capillary forces on immiscible fluid displacement: pore-scale experimental study in a water-wet micromodel demonstrating viscous and capillary fingering, *Energ Fuel*, *25*(8), 3493–3505. https://doi.org/10.1021/ef101732k.
[50] Berga, S., Ott, H. , Klapp, S. A., et al., 2013. Real-time 3D imaging of Haines jumps in porous media flow. *P Natl Acad Sci*, *110*(10), 3755–3759. https://doi.org/10.1073/pnas.1221373110.
[51] Zhao, B., MacMinn, C. W., Juanes, R., 2016. Wettability control on multiphase flow in patterned microfluidics. *P Natl Acad Sci*, *113*(37), 10251-10256. https://doi.org/10.1073/pnas.1603387113.
[52] Chen, Y., Li, Y., Valocchi, A. J., Christensen, K. T., 2017. Lattice Boltzmann simulations of liquid CO2 displacing water in a 2D heterogeneous micromodel at reservoir pressure conditions. *J Contam Hydrol*, in press. https://doi.org/10.1016/j.jconhyd.2017.09.005.

[53] Huang, H., Sukop, M. C., Lu, X., 2015. *Multiphase Lattice Boltzmann Methods: Theory and Application*. West Sussex: John Wiley and Sons Ltd.

[54] Liu, H., Kang, Q., Leonardi, C. R., Schmieschek, S., et al., 2016. Multiphase lattice Boltzmann simulations for porous media applications: a review. *Comput Geosci*, *20*(4), 777–805. https://doi.org/10.1007/s10596-015-9542-3.

[55] Shan, X., Chen, H., 1993. Lattice Boltzmann model for simulating flows with multi phases and components. *Phys Rev E*, *47*(3), 1815–1819. https://doi.org/10.1103/PhysRevE.47.1815.

[56] Shan, X., Doolen, G., 1995. Multicomponent lattice-Boltzmann model with interparticle interaction. *J Stat Phys*, *81*(1-2), 379–393. https://doi.org/10.1007/BF02179985.

[57] Martys, N., Chen, H., 1996. Simulation of multicomponent fluids in complex three-dimensional geometries by the lattice Boltzmann method. *Phys Rev E*, *53*(1), 743–750. https://doi.org/10.1103/PhysRevE.53.743.

[58] He, X., Luo, L., 1997. Theory of the lattice Boltzmann method: From the Boltzmann equation to the lattice Boltzmann equation. *Phys Rev E*, *56*(6), 6811–6817. https://doi.org/10.1103/PhysRevE.56.6811.

[59] Huang, H., Thorne, D. T., Schaap, M. G., Sukop, M. C., 2007. Proposed approximation for contact angles in Shan-and-Chen-type multicomponent multiphase lattice Boltzmann models. *Phys Rev E*, *76*(6). https://doi.org/10.1103/PhysRevE.76.066701.

[60] Sukop, M. C., Thorne, D. T., 2006. *Lattice Boltzmann Modeling: An Introduction for Geoscientists and Engineers*. New York: Springer-Verlag Berlin Heidelberg.

[61] Rabbani, A., Jamshidi, S., Salehi, S., 2014. An automated simple algorithm for realistic pore network extraction from micro-tomography images. *J Pet Sci Eng*, *123*, 164–171. https://doi.org/10.1016/j.petrol.2014.08.020.

[62] Huang, H., Huang, J. J., Lu X. Y., 2014. Study of immiscible displacements in porous media using a color-gradient-based multiphase lattice Boltzmann method. *Comput Fluids*, *93* (10), 164-172. https://doi.org/10.1016/j.compfluid.2014.01.025.

[63] http://www.packomania.com.

[64] http://mechsys.nongnu.org.